ACS APPLIED MATERIALS & INTERFACES

Review

www.acsami.org

Nanocarbon-Scanning Probe Microscopy Synergy: Fundamental Aspects to Nanoscale Devices

Narendra Kurra,[†] Ronald G Reifenberger,*[,‡] and Giridhar U. Kulkarni*[,†]

[†]Chemistry and Physics of Materials Unit and DST Unit on Nanoscience, Jawaharlal Nehru Centre for Advanced Scientific Research, Jakkur PO, Bangalore 560 064, India

[‡]Birck Nanotechnology Center, Purdue University, West Lafayette, Indiana 47907, United States

ABSTRACT: Scanning probe techniques scanning tunneling microscopy (STM) and atomic force microscopy (AFM) have emerged as unique local probes for imaging, manipulation, and modification of surfaces at the nanoscale. Exercising the fabrication of atomic and nansocale devices with desired properties have demanded rapid development of scanning probe based nanolithographies. Dip pen nanolithography (DPN) and local anodic oxidation (LAO) have been widely employed for fabricating functional patterns and prototype devices at nanoscale. This review discusses the progress in AFM bias lithography with focus on nanocarbon species on which many functional quantum device structures have been realized using local electrochemical and electrostatic processes. As water meniscus is central to AFM bias lithography, the meniscus formation, estimation and visualization is discussed briefly. A number of graphene-based nanodevices have been realized on the basis AFM bias lithography in the form of nanoribbons, nanorings and quantum dots with sufficiently small dimensions to show quantum phenomena such as conductance fluctuations. Several studies involving graphitic surfaces and carbon nanotubes are also covered. AFM based scratching technique is another promising approach for the fabrication of nanogap electrodes, important in molecular electronics.

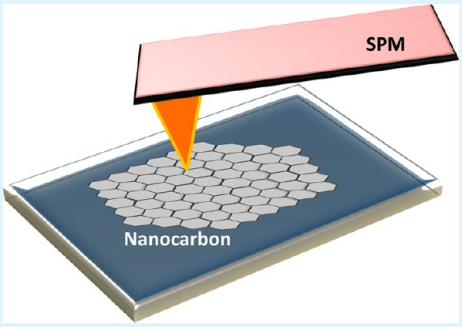

KEYWORDS: *nanocarbon, graphene, bias lithography, scanning probe, electrochemical, quantum devices*

1. INTRODUCTION

In the periodic table of elements, carbon is unique and fascinating, plays a major role in constituting vital life, and is also the most widely employed material in various applications. Graphite (sp^2 bonding) and diamond (sp^3 bonding) are the two crystalline allotropes of carbon, well-known since ancient times for their hugely contrasting properties.[1,2] Because of its versatile bonding possibilities, carbon continues to receive attention as is evident from the research outcome in the past years; fullerenes (since 1985), carbon nanotubes (1991), and graphene (2004) have generated enormous excitement among researchers worldwide.[3−5] The discoveries of fullerenes and carbon nanotubes, while marking the dawn of the "nanocarbon" era, also triggered nanotechnology revolution. The development of top-down and bottom-up strategies in manufacturing nanomaterials, coupled with the invention of scanning probe microscopy (SPM) techniques namely, STM (1981) and AFM (1986) that could image atomic and nanoscale features,[6,7] led to rapid progress in nanotechnology. It may be interesting and worthwhile to revisit the "carbon-SPM" synergy after these many years.

During 1990s, nanolithography based on scanning probes was developed for manipulation and modification of surfaces at nanoscale to study various fundamental quantum mechanical phenomena experimentally.[8−11] Compared to STM, AFM nanolithography is now widely employed for the modification of surfaces locally by application of either mechanical force or voltage bias.[9−11] Force assisted lithography involves the local deformation of material surface via elastic or plastic deformations, mostly used for patterning polymer surfaces.[10] Dip-pen nanolithography (DPN) is a direct write lithographic technique in which various functional molecules can be patterned onto the substrate surface, mediated through the water meniscus formed at the tip-sample interface. DPN has been used extensively to pattern a wide variety of inks such as small organic molecules, polymers, biomolecules, colloids, and metal ions onto surfaces with nanoscale resolution.[12−14]

The water meniscus has also been employed as a local electrolyte to set up a nanoelectrochemical cell under a biased AFM tip, leading to oxidation of surfaces in proximity, popularly known as local anodic oxidation (LAO) or probe-based oxidation.[9−11] There are excellent review articles in the literature discussing various aspects of the local modifications relevant to the specific substrate surface under consideration.[8−11] Although early studies focused on Si surfaces to develop a basic understanding of the kinetics of oxide growth, further work created nanoscale oxide features to act as dielectric layers, etch masks, and templates for specific affinity to functional molecules.[11] Thus, AFM-based lithography techniques could be used for selective functionalization and patterning of the

Received: January 7, 2014
Accepted: April 3, 2014
Published: April 3, 2014

surfaces in addition to the fabrication of complex quantum devices and high-density flash memories.[8−11]

Nanocarbons have been of particular interest in recent years because of their extraordinary physical and electronic properties, making them potential candidates in fabricating functional nanoscale devices.[12−15] To exercise a control over the electronic properties of carbon, the local bonding and functionality must be tuned precisely. Raman scattering has become a leading characterization tool for understanding the crystallinity, bonding and morphology of carbon materials.[16,17] The original idea of obtaining graphene via mechanical exfoliation comes from peeling off top graphene layers from highly oriented pyrolytic graphite (HOPG) using a sticky tape, a technique widely used by the SPM community. Geim and Novoselov performed ground breaking experiments revealing graphene's extra-ordinary electronic properties with linear energy dispersion spectrum.[15,18] Designing various nanostructures on nanocarbon surfaces (including graphene) with desired properties has become an eye-catching approach particularly with SPM via local electrochemical and electrostatic modifications. This approach has led to prototype devices without the need for extensive infrastructure required by photolithographic technologies.[9]

Because of ease of operation, AFM is preferred over STM for patterning of material surfaces. Though STM is successful in fabricating precise nano/quantum scale devices, it lacks the speed and sometimes, reproducibility. Quantum corrals have been fabricated by manipulating atoms using STM tip, which is a fundamental study for mapping out the atomic electronic density waves.[8,11] From an application point of view, STM may not be employable in an effective manner as the active elements are often fabricated on an insulating substrates. AFM, on the other hand, can be employed for patterning not only metal and semiconductor surfaces but also on insulating surfaces including polymers. Further, STM needs an ultra-smooth surface such as Si and HOPG for reliable patterning, which may not be the case with many substrate surfaces which possess intrinsic roughness, sometimes made intentionally. As regards speed of operation, AFM can create patterns much faster compared to STM. Naturally, AFM is the most widely employed technique in this context. This review pertains to AFM bias lithography on carbon surfaces and refers to some notable studies using STM as well. We discuss the aspects of local electrochemical and electrostatic modifications by taking literature examples of various carbon materials—graphite, carbon nanotubes, graphene, and graphene oxide as well as amorphous carbon. As the water meniscus is the starting point for the AFM bias lithography, we first present experimental and theoretical efforts to understand its formation and to characterize its size. The role of the electric field in enhancing the water condensation is also discussed. Further, the role of water as a nanoelectrolyte for modifying various carbon surfaces is discussed. The nanodevices fabricated out of graphene and CNTs using AFM bias lithography are also covered. Graphene in the form of nanoribbons, nanorings, and quantum dots have been carved using AFM bias lithography with the exploration of intriguing electrical transport in these structures. Further, a discussion based on electrostatic charging of graphene, CNTs, and other fluorocarbon surfaces is given in some detail. Finally, the use of AFM probe as a local mechanical probe for scratching the graphene surfaces in order to create nanogap electrodes is also dealt with.

2. CONDENSED WATER BRIDGES BETWEEN TIP AND SUBSTRATE

Water meniscus formation between the AFM tip and the substrate is central to the AFM based electrochemical lithography. Some essential characteristics of the water bridge will be discussed before embarking on the local electrochemical modifications of carbon surfaces and potential implications in sculpting the nanoscale devices.

2.1. Capillarity Induced Water Bridges. Under ambient conditions, hydrophilic surfaces quickly acquire a thin layer of water adlayer, a property that depends on relative humidity (RH). The thickness (h) of these water layers can be inferred from a host of techniques such as infrared spectroscopy, ellipsometry; the mean thickness of water adlayer is found to be typically ∼1 nm at RH of 50%.[19] The above techniques provide only the average properties of water films. On the other hand, STM and scanning polarization force microscopy have been employed to investigate the microscopic structure of the water adlayers on various surfaces under controlled humidity conditions.[19,20] During the early years of AFM, evidence for the formation of a water bridge was inferred from the anomalous behavior of force vs. separation (z) data.[21,22] At a given RH, the onset of a capillary force provided an indirect way of mapping the formation water meniscus between tip and substrate.[23] Theoretical studies for estimating the capillary force have been based on either the macroscopic Kelvin equation or on microscopic models using a Monte Carlo approach[21,24] and density functional theory.[25] Experimentally, the increase in the lift-off force with humidity—observed since the earliest days of AFM—provided good evidence that a water bridge forms between tip and sample. The water bridge between the tip and the sample could assist the transfer of adsorbed molecules from the cantilever to the substrate surface in a desired fashion; this led to the invention of a well-known DPN technique.[12−14] Honschoten et al. have described the basic aspects of capillarity at the nanoscale in their review article.[26] Briefly, the capillary induced water bridge is a metastable state which exhibits anomalous behaviour such as boiling at reduced temperatures and formation of ice at room temperature despite the negative pressures associated with the water bridges.[27] Thermodynamic state of macroscopic water can easily be explained by temperature and pressure effects, whereas the size effects would influence the nanoscale behavior of water.[26,27] Thus, understanding of the capillary forces is very much essential because it has important implications in many distinct areas such as DPN, controlling adhesion forces, and tribological properties of micro/nanoelectromechanical systems (MEMS and NEMS).[27,28]

2.2. Direct Visualization of Water Bridges. When an AFM tip is in contact with a surface, water bridge forms spontaneously under ambient conditions (see Figure 1a). The local curvature of the water meniscus can be described by two geometric parameters R_1 and R_2, which are the principle radii of curvature of the water bridge under consideration (see Figure 1a). For the case of a water bridge at the interface of apex of the tip (approximated by a sphere) and a flat substrate, these two radii (R_1 and R_2) are shown schematically in Figure 1a. In this drawing, both the tip and the substrate are assumed to be hydrophilic and the limiting case is considered when the tip is in contact with the substrate. The radii of curvatures have a sign associated with them that can be determined from the location of the origin of an osculating circle (the dotted lines in Figure 1a)

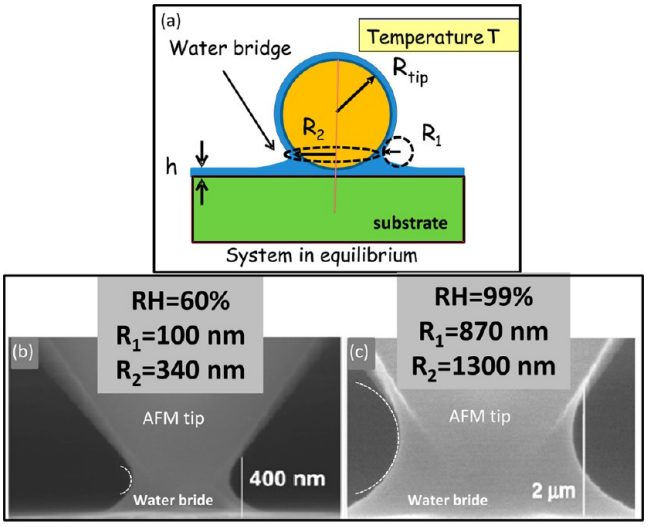

Figure 1. (a) Schematic illustrating the water bridge that forms when a spherical tip is brought close to a flat substrate. The case when the tip is in contact with the substrate is illustrated. R_1 and R_2 are the principle radii of curvature of the water bridge. h is the thickness of the water film. (b, c) direct visualization of the water meniscus at different humidities of 60 and 99%, respectively, in environmental scanning electron microscope. The white dotted curvature represents the negative radius curvature (R_1) of the water meniscus at different RH. Reprinted with permission from ref 29. Copyright 2013 American Chemical Society.

chosen to precisely match to second order the curvature of the surface in a plane. In short, the radius of curvature is positive if the radius lies within the liquid ($R_2 > 0$); it is assigned a negative sign if it lies outside the liquid ($R_1 < 0$). Kelvin radius (R_k) is given by $R_k = (1/R_1 + 1/R_2)^{-1}$, which can establish relationship between the interface curvature at the thermodynamic equilibrium with the ratio of actual and saturated vapor pressure, P/P_o (relative humidity), known as Kelvin equation (see equation1).

$$(RT/\gamma V)\ln(p/p_o) = 1/R_k \quad (1)$$

where R is the universal gas constant, T the absolute temperature, γ is the surface tension, V is the molar volume, p_o the normal vapor pressure of the liquid, and p is the pressure acting outside the curved surface. According to the Kelvin equation, a concave meniscus with a negative curvature (from eq 1) may form at any RH and the size of the water bridge due to capillarity can be predicted.[26]

To visualize the water meniscus formation, Weeks et al. have employed an environmental scanning electron microscope with an AFM attachment and have directly estimated the size of water bridge under different humidity conditions (Figure 1b, c).[29] The vertical and lateral dimensions of the water meniscus are enhanced with increasing RH (see Figure 1b, c). The height of the meniscus was determined as the perpendicular distance from the substrate surface to the condensate/cone contact line. The contact line is where the change in angle between the meniscus and the cantilever tip is observed. It was found that the height of the meniscus ranged between 100 to 1200 nm for RH values between 70 and 99%. A few studies to validate the Kelvin equation at the nanometer length scale have been reported, and they indicate the validity of the Kelvin equation for menisci with a mean radius of curvature as low as 4 nm.[30] When the water gets confined into a small liquid bridge, it exhibits properties different from that of bulk, and indeed, it is well-documented that icelike structures could be formed in the first few layers of water adsorbed onto a solid substrate.[19] The properties of the water menisci are highly dependent on local variations in structure as well as the compositional properties of the sample and tip. It is possible that contamination from the tip or substrate may cause a change in the surface tension of water from the accepted value of 0.072 J/m^2, which may influence the properties of water bridges.[31,32]

2.3. Influence of Electric Field on Water Condensation.

Water molecule has an electric dipole moment with a value of 6.2 × 10^{-30} C m (1.8 D), making water highly polar (dielectric constant = 80). This implies that water molecules can be controlled via external electric fields. Water molecules exhibit partial alignment in high electric fields with a decrease in their molecular rotational kinetic energy as well as their diffusivity. These effects change the free energy of condensation and facilitate, for example, the nucleation of ice layers on the surface of electrified wires.[33]

Figure 2 summarizes the conditions for water meniscus formation when an AFM tip is biased, either in contact or in the

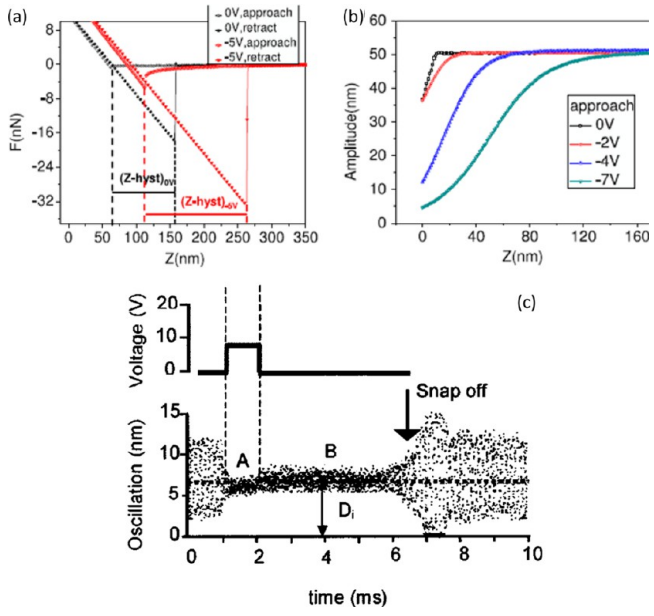

Figure 2. Estimation of capillary force in contact and dynamic modes of AFM in the presence of an electric field. (a) Static force−displacement data showing the enhancement in the size of water bridge when the tip is biased. (b) Reduction in the amplitude through capillary and electrostatic forces for different tip bias during tapping mode operation. (c) Monitoring the tip oscillation with respect to the application of voltage pulse during the noncontact mode of operation at RH of 55% and applied voltage pulse is shown on the top. Reprinted with permission from refs34 and 35. Copyright 2011 Institute of Physics and 2002 American Institute of Physics.

dynamic mode. The water meniscus formation can primarily be influenced by capillary and long-range electrostatic forces. The change in cantilever deflection and amplitude provides indirect information about the kinetics of formation of the water bridge. Even at a RH of 10%, the water meniscus forms spontaneously between a hydrophilic tip and a hydrophobic surface without application of voltage bias. However, an electric field could enhance water condensation at the tip−substrate contact because of the electrostatic attraction of polarized water molecules, a process often referred to as field enhanced water condensation. As a result, the biased AFM tip can experience two

dx.doi.org/10.1021/am500122g | ACS Appl. Mater. Interfaces 2014, 6, 6147−6163

attractive forces, namely electrostatic and capillary. In Figure 2a, the increase in lift-off force as the tip bias increases indicates the formation of a water meniscus, whereas long-range attractive electrostatic forces are evident from amplitude−displacement data (Figure 2b).[34] Amplitude−displacement (A−Z) data provides an insight into the reduction in the amplitude of the cantilever when approaching to the sample surface. The onset of decrease of the amplitude was observed at higher Z values when the tip was biased, compared to the unbiased tip (shown as black curve in Figure 2b). The long range electrostatic attractive forces are more pronounced as the tip bias is increased from −2 to −7 V (see Figure 2b). Thus, the onset of the amplitude reduction depends on the magnitude of voltage applied on the tip as seen in Figure 2b, due to increase in the attractive forces between the tip and the sample at higher tip voltages. Garcia et al. have observed the formation of a water neck when a voltage pulse was applied to the AFM tip during noncontact mode of operation.[35] The applied voltage (above a certain threshold voltage, V_{th}) induced the formation of a water bridge causing the reduction in the amplitude of the cantilever (Figure 2c). After turning off the voltage, the water bridge breaks, allowing the cantilever to recover its original oscillation amplitude (see B in Figure 2c).

Sacha et al., have proposed an analytical model which explains the enhancement in the formation of water menisci and bridges between the tip and sample in relation to the electric field near a sharp tip in humid environments.[36] Cramer et al., performed molecular dynamics simulations to describe the formation of a water bridge induced by an electric field.[37] Restriction of orientational degrees of freedom (confinement) of water dipoles at the interfaces leads to polarizability that depends on the shape of the water system. In the absence of electric field, the configuration of water system was seen as a droplet with an average contact angle on silicon dioxide surface of 40° (Figure 3a). Up on the application of electric field (above 1.25 V nm^{-1}), the field perpendicular to the surface polarizes and distorts the outermost water layer, leading to the change of droplet shape (Figure 3b). As this process continues, finally a water pillar is formed at higher electric fields (Figure 3c). The increase in the height of the water bridge (h_z) has also been investigated at varied electric fields (Figure 3d). Molecular based explanation provides an insight about the interplay between the orientation of water dipoles and the strength of hydrogen bonding with respect to the applied electric field. It has been demonstrated that below a certain electric field 1 V nm^{-1}, water molecules remain in the droplet configuration due to restriction for re-orientation of the dipoles. At the threshold field of 1.2 V nm^{-1}, the outermost dipoles start aligning with the field with the weakening of the hydrogen bonds among the molecules underneath. This dipole alignment can trigger the formation of the water bridge in which most of the interface is parallel to the field. This leads to a condition where the system fulfills the double requirement of retaining the interfacial hydrogen bond network with orientational polarization. Above the critical electric field strength, the electrostatic pressure overcomes the surface tension, causing the rise of the pillar. Thus, the model could explain the threshold voltage and hysteresis behavior during the formation of water bridge.[36−38]

2.4. Electric Field-Induced Water Condensate Structures. Experimentally, attoliter (1×10^{-18} L) quantities of water have been nucleated on a carbonaceous surface using a positively biased AFM tip in tapping mode (RH = 45%). The carbonaceous platforms were fabricated by a technique called electron beam induced carbonaceous deposition (EBICD).[39] The AFM

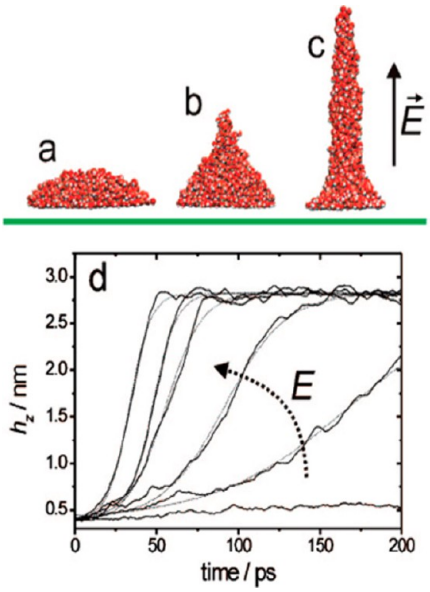

Figure 3. (a−c) Change in the shape of the water bridge with respect to the applied electric field on a hydrophilic surface. Snapshots from the simulation at E_z = 2.0 V nm^{-1}(oxygen, red; hydrogen, white). (d) Growth of the water bridge was investigated at different electric fields (2.25, 2.0, 1.75, 1.5, 1.25, and 1.0 V nm^{-1}). At higher electric fields, the shape of the water changes from a droplet to a pillar shape. Reprinted with permission from ref 37. Copyright 2008 American Chemical Society.

topography of the water corral-like structure is shown in Figure 4a. The water feature evaporates at a rate of 2 aL/min. After complete evaporation of the water structure, the carbonaceous surface is found to be neat as before, ruling out possible electrochemical reactions under the experimental conditions

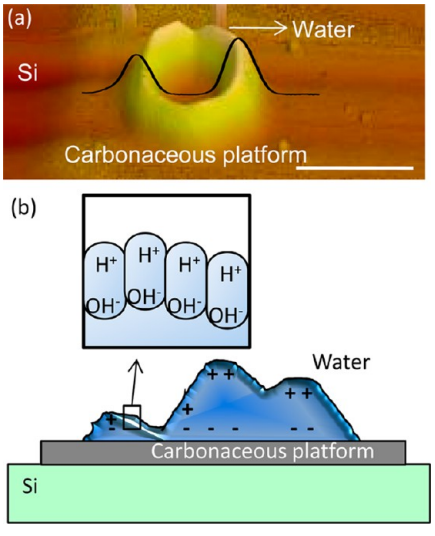

Figure 4. (a) AFM topography image and corresponding line profile of a hexagonal water pattern showing the unusually sharp local water morphology that can be achieved using AFM-induced electrocondensation. The horizontal scale bar is 2 μm and the maximum height of the water feature is 27 nm. (b) Schematic illustrating the presence of local tip-induced charge and polarization in the water, which contributes to the anomalous droplet shapes and the observed evaporation characteristics. Reprinted with permission from ref 39. Copyright 2010 Tsinghua University Press and Springer−Verlag.

adapted. Surprisingly, the structure shown in Figure 4 showed little tendency to collapse into a rounded droplet. The overlapping z-profile shows unusually sharp local morphology and corrugations of the water condensate. This is illustrated with the schematic shown in Figure 4b. The formation of water condensate structures on EBICD surface was attributed to its novel surface functionality. The carbonaceous surfaces fabricated using e-beam irradiation host many functional groups resulting from complex reactions of residual hydrocarbons in the presence of moisture. A positively biased AFM tip can cause polarization of the surface functional groups on EBICD and electrostatic clamping of water molecules, leading to nucleation of water features (Figure 4b). One important aspect of these condensate structures is the evaporation kinetics; attoliter water droplets have shown an unusual slow evaporation kinetics (2 aL/min.) Confined water droplets combined with localized charges arising due to the alignment of water dipoles under the electric field may result in special properties different from the macroscopic behavior of water condensates. The transient nature of the water condensate structures may be employed as reversible local doping structures on nanocarbon surfaces for sensing some specific molecules of interest at the nanoscale. Thus, controlling and manipulating condensate structures employing electric field may have implications in the fields of nanosensors and AFM nanolithography techniques.

3. LOCAL ANODIC OXIDATION (LAO)

LAO is a process that takes place in a simple nanoelectrochemical cell in which AFM tip serves as a cathode, the water bridge formed between the tip and surface as electrolyte, and the substrate serves as anode. LAO resembles conventional anodic oxidation except that the former relies on 1×10^4 to 1×10^5 water molecules, whereas the latter uses Avogadro's number ($\sim 6 \times 10^{23}$) of electrolyte molecules in order to oxidize the material surfaces. The water bridge is usually formed either by mechanical contact between tip and sample surface or through the application of an electrical field in the case of dynamic modes of operation. The applied voltage bias of few volts generates an electric field of 1×10^9 to 1×10^{10} V/m, which induces the ionization of water molecules, leading to the generation of oxidative species (OH^-, O^-) which cause the oxidation of material surfaces locally, known as probe based anodic oxidation or LAO.[10,11] The high aspect ratio of the AFM tip further concentrates the electric field upon application of a bias voltage. Besides the electrochemical modifications, such extremely high electric fields can initiate various local physical and chemical processes such as electrostatic charging, field emission, Joule heating, explosive discharge, nanoexplosion, and shock wave generation.[9−11]

The interest in LAO is to develop ultramicroelectrodes (UMEs) in electrochemistry. UMEs have been intensively studied since the 1990s because they enable unprecedented spatial and temporal resolution in electrochemical measurements.[40] UMEs have combined high current densities with low measuring currents to reveal new effects because of a time-dependent change in mass transport in which traditional, one-dimensional diffusion fields are replaced by rapidly varying fields that are spatially inhomogeneous.[40] Many of the initial LAO experiments have been performed on Si surfaces to gain a basic understanding of oxide growth kinetics and optimization of experimental parameters. The anodic oxidation of semiconductors and metals can be explained through the following chemical reactions proposed by Sugimura and Nakagiri.[41]

$$\text{At anode: } M + nH_2O \rightarrow MO_n + 2nH^+ + 2ne^- \quad (2)$$

$$\text{At cathode: } 2H^+(aq) + 2e^- \rightarrow H_2(g) \quad (3)$$

where M represents the anode (a metal or Si surface) at which oxidation takes place, whereas the tip is cathode where hydrogen gets liberated. LAO on a Si surface produces SiO_2 which has a greater volume compared to Si, leading to the formation of a protruded oxide feature on the surface. Alternatively, depressions on Si can be formed through wet chemical etching of SiO_2 using dilute HF (Figure 5a). The LAO technique has been employed

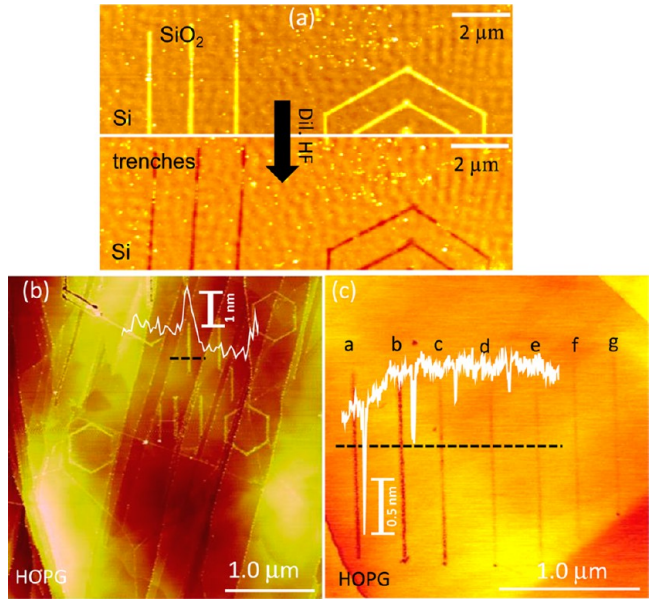

Figure 5. (a) Local anodic oxidation of Si surface followed by etching in dil. HF. (b) Electrochemical modification (oxidation and etching) of graphitic layers with a negatively biased AFM tip at a relative humidity (RH) of 35%. AFM topography (shown in b) of the oxidized patterns on the graphite surface in the form of lines and hexagons, achieved with a tip bias of −8 V in tapping mode. (c) Trench patterns of different depths (labeled a to g) on graphite surface with biases ranging from −8 to −6.8 V in contact mode (voltage step of 0.2 V). The corresponding *z*-profiles are given. Reprinted with permission from ref 34. Copyright 2011 Institute of Physics.

widely for the oxidation of various surfaces such as metals (Ti, Ta, Al, Mo, Ni, Nb), semiconductors (SiC, III−V semiconductors), dielectrics (Si_3N_4, perovskite films), and self-assembled monolayers and carbonaceous films.[10]

The AFM mode of operation is very important during the AFM bias lithography. It is found that during contact mode lithography which requires a continuous voltage bias, there is a buildup of space charge within the oxide which limits the further growth of the oxide. Dynamic AFM modes such as tapping and non-contact techniques could produce high-aspect-ratio oxide features because of the pulsing nature of the applied bias, which minimizes the width of the meniscus.[42] It was also reported that the attachment of nanotubes to the AFM tip resulted in 10 nm wide oxide lines at scan speeds up to 1 mm/s.[43]

3.1. LAO on Si and Metal Surfaces. In 1990, Dagata and co-workers observed the modification of hydrogen-terminated silicon surface through application of a bias voltage between an STM tip and the surface.[44] The composition of the modified region was found to be silicon oxide, confirmed through secondary ion mass spectrometry (SIMS). This phenomenon

has been attributed to the local oxidation of the Si under the electric field from the STM tip.[44] In 1993, similar observations were made by employing AFM, which caused the local oxidation of Si(111) surfaces.[41,45] Typically, conducting AFM tips such as Pt/Ir, Au, W_2C-coated, and heavily doped Si probes have been employed for the local oxidation of surfaces in both contact and dynamic modes.

As the LAO technique forms oxides that are typically insulators, they have been employed as local dielectric barriers and masks for selective etching.[11] The oxide features were also employed as templates for the selective attachment of functional molecules in an electrostatic manner. LAO by scanning probe techniques (STM and AFM) have also advanced as important tools for studying phenomena such as coulomb blockade and quantum conductance in addition to finding use in the fabrication of nanoscale electronic and mechanical devices. AFM lithography on various surfaces with different kinds of modifications have been provided in the review articles.[8−11] The devices fabricated on the basis of LAO are quite large, and include data storage memories, side-gated field effect transistors, single electron transistors, and various other quantum devices.[46,47] LAO sites have also been exploited as binding sites for the growth of biomolecules and conjugated materials besides its role as an etch mask.[8−10] For example, LAO has also been employed to fabricate/write alternating insulating and semiconducting rings, arrays of dots, and even the first ten lines of "Don Quixote" (the famous Spanish novel).[11]

AFM-based bias lithography has also been employed in the case of polymeric films where the intense electric fields can cause local ablation due to joule heating while the mild electric field causes electrochemical or electrostatic modifications.[48−50] Nanoscale explosion and shock wave propagation were also observed in case of polymers and semiconductor surfaces under higher humidity and bias conditions.[51−53] Besides the above mentioned local chemical modifications, AFM bias lithography has also been employed to write charge patterns on the electret films,[54] polymers,[55] fluorocarbon films,[56] and even on $LaAlO_3$/$SrTiO_3$ heterostructures.[57] Thus, AFM bias lithography became an effective tool to cause various kinds of local modifications depending on the material surface and operating conditions.

Though much of the earlier reports were mainly focused on Si surfaces and to some extent various metal surfaces, due to recent interest in fabrication of carbon-based devices, SPM lithography has become a popular tool for realizing carbon nanodevices directly. The basic difference between the Si and C substrates is that Si can only be oxidized, whereas carbon can be either oxidized or etched during SPM lithography. As the electronic properties of carbon are very sensitive to the local electrochemical modifications, SPM lithography can offer the possibility of fabricating nanocarbon devices with tunable electronic properties. In addition, SPM lithography provides a resist-free method for fabricating carbon nanostructures. The advantages are far-reaching because the intrinsic electronic properties remain preserved, unlike other lithographic techniques such as electron-beam lithography and photolithography, which involve resist coating with multiple steps of chemical processing. Nanofabrication with scanning probe microscopes provides a widely accessible method for high resolution nanofabrication with a precision approaching atomic (0.1 nm) dimensions.

3.2. Electrochemical Modification of Carbon Surfaces. The electric field applied between a tip and a carbon surface in the presence of a water bridge may cause either oxidation or etching, depending on the RH, the magnitude of applied bias, the duration of the applied voltage, and the AFM mode of operation. Oxidation involves the formation of protruded oxide features, whereas etching involves the volatilization of carbon locally, resulting in the formation of trenches. Electrochemical oxidation and etching of various carbon surfaces such as graphite, amorphous carbon, carbon nanotubes, and graphene are discussed below.

3.2.a. Graphite Surface. In a classic study (Figure 5), AFM bias lithography was performed on an HOPG surface with a negative tip bias of −8 V at a RH of 35%.[34] Lithography in tapping mode was found to oxidize the HOPG surface, producing local topographic features that protruded above the HOPG surface with a typical height of 1.0−1.5 nm as determined from the corresponding *z*-profile (see line scan in Figure 5b). The lithography performed in contact mode with a negative tip bias of −8 V resulted in the formation of trenches (see Figure 5c). Typically, the apparent depth of trench patterns can be obtained as low as 0.4 to 1.5 nm in the voltage range of −6.8 to −8 V applied on the AFM tip (see *z*-profile in Figure 5c) at RH of 35% in the contact mode. It is possible to get different trench depths based on AFM bias and RH conditions. A number of such studies on the oxidation or etching of the HOPG surfaces under different experimental conditions have been reported.[58−63] Graphite patterning was also performed in controlled gas environments, which included the vapors of methyl alcohol, oxygen, and isopropanol.[64] Most of the studies were focused on the basic understanding of local electrochemical modifications under a variety of experimental conditions such as magnitude of the tip bias, RH, and AFM mode of operation.[61−63]

Under mild experimental conditions (tip bias < 8 V and RH < 40%), partial oxidation of the graphite surface results in the formation of protruded oxide features. Higher tip bias and RH results in complete oxidation which causes the gasification of carbon, resulting in the formation of trenches. According to Pourbaix diagram of carbon, it is possible to etch (complete oxidation) the carbon surface at lower voltages but only partial oxidation (formation of surface functional groups) is favorable according to chemical kinetics.[34] This important result predicts the formation of surface functional groups such as carbonyl (C═O), carboxyl (COOH), and epoxy (CH−CH_2−O). The appearance of such functional groups can be treated as a partial oxidation represented by the following chemical reactions.

$$C_s + H_2O + \text{E-field} \rightarrow C{=}O(\text{carbonyl}) \downarrow + H_2 \quad (4)$$

$$C_s + 2H_2O + \text{E-field} \rightarrow CO_2 \uparrow + H_2 \quad (5)$$

Etching of carbon surface is due to the complete oxidation where the sufficient supply of the oxidative species converts solid carbon (C_s) into gaseous CO and CO_2.

Typically, graphite is a widely employed material in the field of electrochemistry as a counter electrode due to its high electronic conductivity and excellent electrochemical stability. Under normal conditions, the anodic oxidation of carbon using water as an electrolyte is a slow process but it can be accelerated by high electric fields between the biased tip and carbon surface. In reality, both oxidation and etching of carbon surfaces may take place simultaneously resulting in the localized features that contain carbon atoms modified by oxy-functional groups because of incomplete reactions. Thus, AFM bias lithography has become a reliable tool for the local electrochemical modifications of the carbon surfaces in a controlled manner.

Similar electrochemical modifications may be expected for other carbon surfaces such as amorphous carbon, carbon

nanotubes and graphene. To explore the possibilities, AFM bias lithography was performed on amorphous carbon surfaces created by various methods such as electron beam induced deposition and sputtering. Local modification of the chemical composition of the carbonaceous films through AFM bias lithography, followed by etching resulted in the fabrication of high-resolution semiconductor features of the order of ∼22 nm wide.[65] Electric field-induced electrochemical modifications have also been observed in the amorphous carbon thin films.[66] Various electrochemical and physical modifications such as oxidation and charge writing have been observed on the carbonaceous deposits produced by electron beam irradiation depending on the experimental conditions employed.[67,68]

3.2.b. Local Electrochemical Modifications on Carbon Nanotubes. AFM bias lithography has also been employed to cause the local electrochemical modifications of carbon nanotubes.[69−71] Kim et al., have employed AFM as a tool for cutting multiwalled carbon nanotubes into the fragments and also probed the mechanism behind their findings.[69] Park et al., employed AFM bias lithography to modify the electrical properties of carbon nanotube devices by creating breaks and nicks on the carbon nanotube surface through applying voltage pulses using a metal-coated AFM tip in order to create tunnel barriers along a nanotube.[70] These methods have been employed to make single nanotube devices by cutting nanotubes or by creating small quantum dots with large charging energies by placing two tunneling barriers 50 nm apart along a nanotube.

AFM bias lithography was performed on a CNT which was connected to two metal electrodes (Figure 6a). By applying voltage pulses on the AFM tip (26 V with durations of 100 ms and 50 ms), the CNT can be cut or nicked at defined locations on the CNT surface (see Figure 6b). The size of gap between two cuts has been controlled by the amplitude and duration of the voltage pulses. The extent of cutting can be monitored through conductance (G) of the CNT which may decrease to zero suddenly. A quantum dot along the length of the CNT was created through nicking process (see the schematic in the lower inset of Figure 6c). The initial conductance (G) of CNT was $0.1e^2/h$ and dropped to $0.05e^2/h$ after the first nick and finally to $0.025e^2/h$ after the second nick, which was positioned 50 nm apart by application of voltage pulses of 26 V for 10 ms. This indicates that the formation of two barriers in series with approximate conductances of 0.1 and $0.05e^2/h$ each. In Figure 6c, conductance with a unit of e^2/h is plotted against gate voltage V_g at T = 20 K. The observation of the Coulomb oscillations can be attributed to the addition of single electron to this quantum dot. The differential conductance (dI/dV) map of this device as a function of V_g and source−drain voltage (V_{sd}) is represented in gray scale (see upper inset of Figure 6c). From these coulomb diamonds, the charging energy is found to be $e^2/C \approx 75$ meV and this value is comparable to that observed in the case of CNT quantum dots of length 50 nm produced by ultrasonication method.[70] However, small CNTs obtained by ultrasonication or other methods pose a challenge while establishing electrical contacts. But with AFM bias technique, one can easily create tunnel barriers on any length of nanotube without having much trouble. CNT quantum dots can also be made by mechanical techniques. Mechanical techniques have been employed to break or bend for creating tunnel barriers involving nanoobjects. However, as mechanical techniques rely on large forces (0.1−10 μN), this may lead to the disruption of the electrical contact between the CNT and the metallic contacts.[70] This brings out the capability and the importance of the AFM bias lithography technique while fabricating complex architectures such as multiple quantum dots, CNT−CNT junctions and Aharonov−Bohm rings. The nanogaps formed on CNT surfaces by cutting with AFM lithography could also be used as electrodes for probing the electrical characteristics of nanocrystals or single molecules suspended across the nanogap. Thus, AFM bias lithography on CNT surfaces can give rise to many interesting opportunities in studying fundamental aspects besides the fabrication of advanced nanoscale devices.

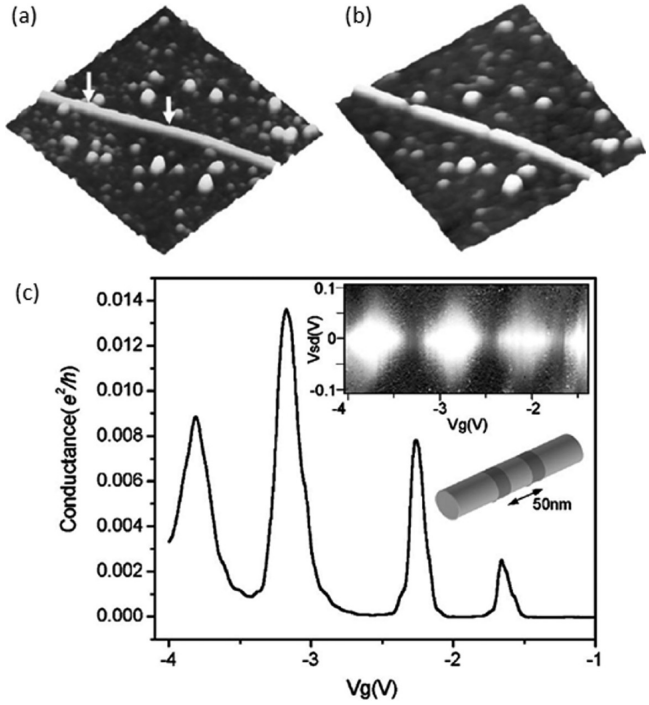

Figure 6. Three-dimensional AFM image of the CNT (height of 3 nm) on the oxide surface (a) before and (b) after cutting by applying two voltage pulses (amplitude of 26 V) with a duration of 100 (left) and 50 ms (right). The regions are marked by arrows in a. Scan size of 500 × 500 nm. (c) Quantum conductance as a function of gate voltage of a CNT quantum dot at 20 K. Inset shows the schematic of the CNT quantum dot, where the dark bands at a separation of 50 nm represents tunneling barriers created by nicking. The map of differential conductance (dI/dV) as a function of V_g and V_{sd} at T = 20 K is shown in the upper inset of c. Low and high values of dI/dV are represented with white and black regions of the differential conductance map. Reprinted with permission from ref 70. Copyright 2003 American Physical Society.

3.2.c. Graphene Nanodevices. Graphene, a 2D flat material, has been studied extensively in recent years because of its promising electronic and optoelectronic properties and not surprisingly, a number of studies using AFM-based lithography have been published. In principle, graphene is a semi-metal with a linear energy spectrum that is expected to exhibit many unusual properties.[72,73] However, most of the electronic applications require the presence of an energy band gap. The band gap can be opened by carving the graphene in the form of graphene nanoribbons (GNRs) which lead to lateral confinement of charge carriers. The electronic properties of the GNRs are quite sensitive to the geometry of the edge structure, its functionality, and overall quality.[74,75] State-of-art lithographic techniques such as electron beam lithography and plasma etching have been employed but the intrinsic electronic properties of the devices are

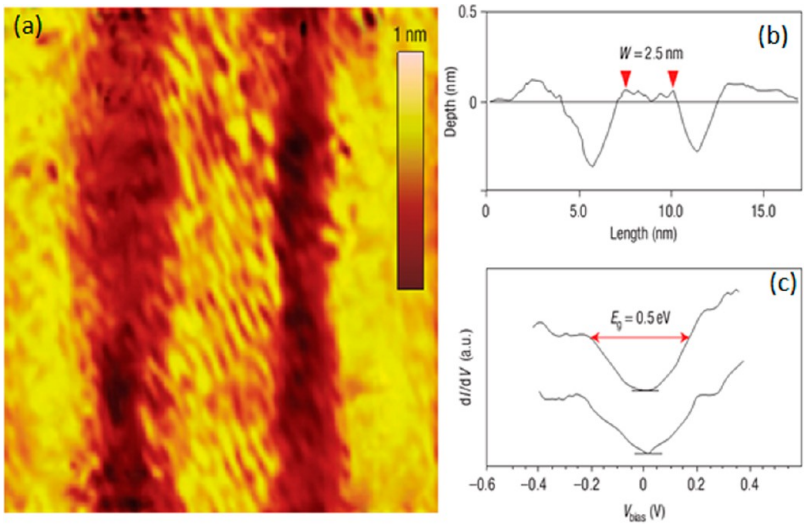

Figure 7. STM lithography for the fabrication of GNRs: (a) STM image (scan area, 15 × 15 nm^2), 1 nA, 100 mV) of an armchair GNR (width of 2.5 nm). (b) STM *z*-profile showing the real width and depth of the GNR. (c) STS spectra collected from the narrow ribbon with an energy gap of about 0.5 eV (zero DOS marked by horizontal lines). Reprinted with permission from ref 78. Copyright 2008 Nature Publishing Group.

often compromised because of the unwanted presence of residues.[76,77]

SPM lithography offers a viable method for resistless, controlled patterning of graphene nanodevices via local electrochemical modifications. Levente et al. have employed STM lithography to sculpt graphene nanoribbons (GNRs) out of a single graphene flake.[78] STM lithography was successfully employed to fabricate GNRs with typical widths of few nanometers in the form of armchair and zig-zag configurations. The finest GNR (width of ∼2.5 nm) was fabricated by applying a tip bias of 2.28 V at a tip velocity of 1 nm/s (see Figure 7a, b). The energy band gap of the same GNR was estimated through scanning tunneling spectroscopy (STS) measurements and found out to be 0.5 eV (Figure 7c). As this value is comparable to the band gap of Ge (0.67 eV), GNR can be the potential candidate material for the future electronic devices.

Compared to STM-based lithography, AFM is relatively easy and takes less time for the fabrication of GNRs. AFM bias lithography has been employed for patterning epitaxial graphene on SiC and also mechanically exfoliated graphene.[78,79] Further, it has been employed for the fabrication of graphene nanodevices such as GNRs, nanorings and quantum devices.

Masubuchi et al., have employed AFM bias lithography to fabricate a GNR with a width of 800 nm (Figure 8a).[80] The electronic properties of the device were investigated through electric field effect and Hall measurements. The transfer characteristics showed ambipolar behavior with a charge neutrality point close to zero, $V_{Dirac} \approx 5$ V (see Figure 8b). The electron mobility (μ) of this device was 7000 cm^2/V s, which is comparable to μ of pristine single-layer graphene devices. This indicates that the conducting channel of graphene is largely unaltered during LAO lithography. Figure 8c shows channel conductance (G) as a function of V_g measured at T = 4.2 K in a magnetic field of B = 9 T. The conductance plateaus were observed at quantized values of $G = 2e^2/h$, $6e^2/h$, $10e^2/h$, and $14e^2/h$ for V_g values of 12, 22, 35, and 45 V, respectively. The quantum Hall plateaus obey the sequence $G = 4(N + 1/2)(e^2/h)$, where N is an integer, representative for the half-integer quantum Hall effect.

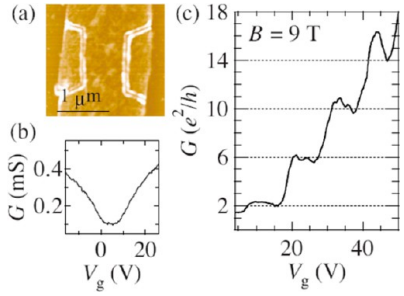

Figure 8. (a) AFM topography of the bar-shaped device fabricated in single-layer graphene. (b) Transfer characteristics of the device (channel conductance (G) versus gate voltage (V_g) measured at T = 4.2 K in a zero magnetic field. (c) G as a function of V_g measured at T = 4.2 K at a magnetic field of 9 T. Reprinted with permission from ref 80. Copyright 2009 American Institute of Physics.

Besides the fabrication of GNRs, AFM has also been employed to fabricate nanoring devices (Figure 9a, b).[81] In a study reported by Weng et al., AFM has been employed for the fabrication of graphene nanoring devices which showed universal quantum conductance fluctuations.[81] To electrically isolate the nanoring device, two long trenches were subsequently drawn from the circumference of the ring outward to the edges of the flake. The nanoring device (width of the conducting region is about 220 nm) showed reproducible conductance fluctuations as a function of magnetic field (B) or gate voltage (V_g) (see Figure 9c, d) at temperatures T < 50 K. These fluctuations can be attributed to the universal conductance fluctuations (UCF) in such a nanoring device.

In addition to the etching of graphene into GNRs and nanorings, Masubuchi et al., employed AFM to fabricate graphene/graphene oxide (GO)/graphene junctions and showed that the properties of the junctions can be tuned from semi-insulating to semi-conducting depending on the extent of oxidation.[82] This study has brought out the precise control possible with the process which is reflected in the fabricated devices. To fabricate graphene/GO/graphene junctions, a biased AFM tip was moved from one edge of the graphene flake to the other edge (Figure 10a). The GO region is observed as a dark

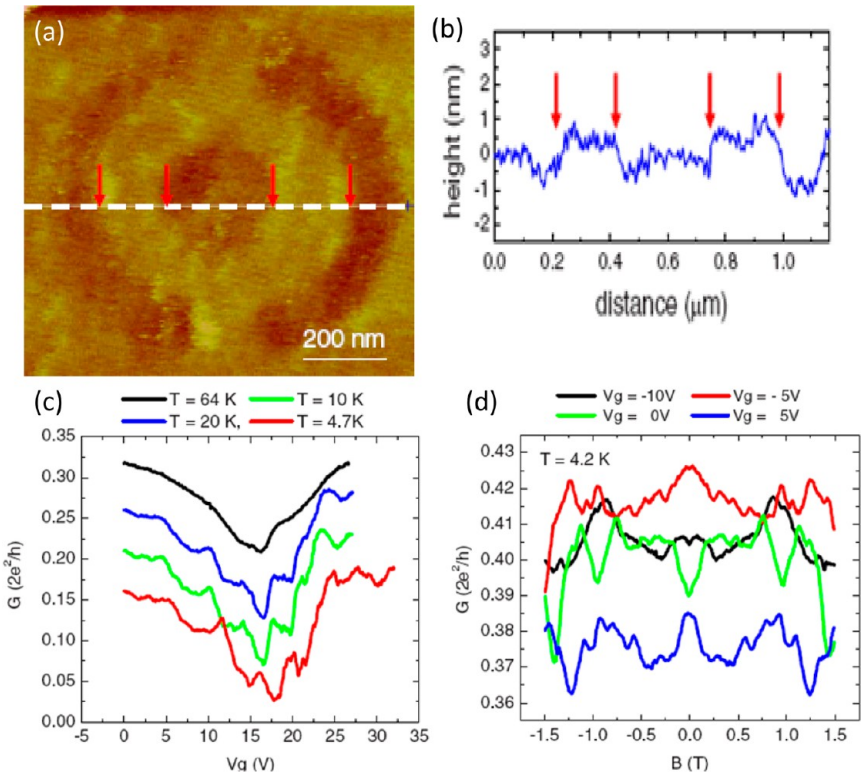

Figure 9. (a) Nanoring (inner and outer radii of ~160 nm and ~380 nm, respectively) patterned on a graphene flake using local electrochemical etching. (b) *z*-profile corresponding to the dashed line in a. (c) Conductance fluctuations as a function of gate voltage at different temperatures for the nanoring device in a. (d) Magnetoconductance of the nanoring device with different gate voltages measured at 4.2 K. Reprinted with permission from ref 81. Copyright 2008 American Institute of Physics.

strip in the friction image; the bright region corresponds to the pristine graphene (see Figure 10b). The width (w_b) of the GO can be controlled through the tip bias (V_{tip}) (see Figure 10c). It was observed that w_b increases from 20 to 50 nm as $|V_{tip}|$ varies from 5.5 to 9.0 V. The transfer characteristics of the pristine graphene (dotted curve, Figure 10d) were compared with the G/GO/G junctions created with different $|V_{tip}|$. The conductance of the G/GO/G junctions is gradually decreasing for the devices created at higher tip bias $|V_{tip}|$ yet maintaining the V-shaped dependence like pristine graphene. For a tip bias $|V_{tip}|$ greater than 8 V, the conductance is completely suppressed (see Figure 10d) and no longer modulated by V_g. The plot of minimum conductance (G_{min}) as a function of $|V_{tip}|$ is shown in Figure 10e. This study nicely illustrates the tunability of the conductance of G/GO/G junctions according to $|V_{tip}|$. The conductance of G/GO/G junctions is modulated by the extent of oxidation, allowing the tuning of the junction properties from semiconducting to semi-insulating.

Park et al., have shown that graphene can also be hydrogenated locally through application of positive tip bias polarity, besides the oxidation and etching using a negative tip bias.[83] Thus, depending on the tip bias polarity and its magnitude, graphene can be oxidized, etched, or reduced, a result that is useful to create local conducting or insulating regions.

The ability of AFM bias lithography to create both hydrogenation and oxidation patterns on graphene is illustrated in Figure 11. The hydrogenated (blue dashed lines) and oxidized lines (red dashed lines) were made on graphene using a substrate bias of −10 and +7 V at tip velocity of 0.1 μm/s respectively (see FFM image, left panel in Figure 11a). In this case, the bias was applied to the sample where negative and positive sample bias would result in hydrogenation and oxidation of the sample respectively, in contrast to the response exhibited with regard to tip bias polarity, which is just the opposite. The corresponding conducting AFM (cAFM) map is shown in the right panel of Figure 11a. The hydrogenated lines were fabricated with sequentially increased loading force from 1 to 4 nN, in order to increase the coverage of hydrogen atoms on graphene. The cAFM mapping revealed the highly insulating nature of hydrogenated or oxidized regions of graphene compared to its surroundings. Conducting gaps with sub-20 nm features were created using this technique (see Figure 11b).

Novoselov et al. employed AFM to fabricate graphene quantum dot devices with controllable ambipolar transition of a single hole, through an empty QD, to a state with a single electron.[84] Figure 12a shows the topography of the QD structure fabricated by AFM bias lithography (tip bias of −7 V, RH ~ 70%, scanning speed, 200 nm/s). Oxide regions appear as dark while the pristine graphene as bright in the friction images (Figure 12b). This study has demonstrated the potential of the AFM lithography technique in sculpting graphene into active channel material QD and also passive source, drain and side gate electrodes. This can eventually lead to the possible development of all-graphene based electronics. The width of the lines can be controlled through RH with a minimum width down to ~15 nm obtained at relatively low humidity. The electronic nature of the QD device was examined at different temperatures by applying back gate voltages. The conductivity showed a strong distortion from an expected V-shape and in the voltage window from 33 to 41 V, the conductivity falls well below one conductivity quantum (e^2/h). In this range, several sharp conductivity peaks are observed and may be related to the quantized transport through

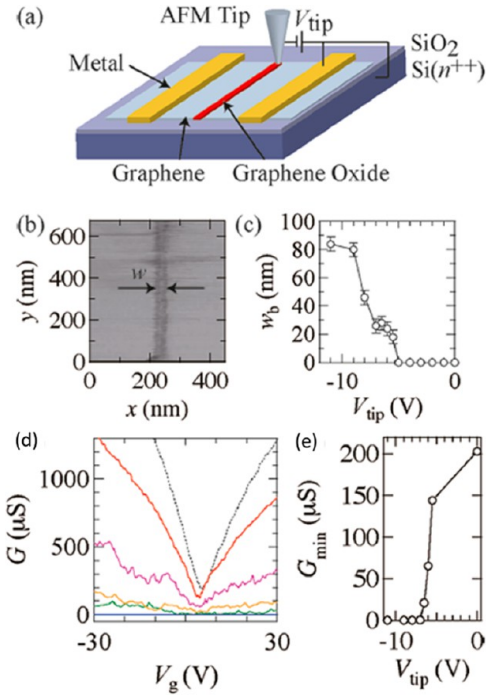

Figure 10. (a) Schematic setup showing the fabrication of graphene/GO/graphene junctions based AFM-bais lithography. (b) Dark strip in the friction image correspond to GO (V_{tip} = −8.0 V, scan speed (v_s) of 50 nm/s) and bright region is for the pristine graphene. (c) Width (w_b) of the GO strip as a function of tip bias voltage for v_s = 50 nm/s. (d) Transfer characteristics of the pristine graphene (dotted curve) and G/GO/G junctions (solid curves) as a function of gate-bias voltage V_g at T = 4.2 K. The bias voltages applied to the AFM cantilever were varied as V_{tip} = −5.5 (red), −6.0 (magenta), −6.5 (yellow), −7.0 (green), −8.0 (blue), −9.0 (purple), and −11.0 V (dark green) (from top to bottom). (e) Minimum conductivity G_{min} as a function of tip bias (V_{tip}) at T = 4.2 K. Reprinted with permission from ref 82. Copyright 2011 American Chemical Society.

the QD device (see Figure 12c). As the quantum point contacts (QPCs) are narrow constrictions, the transmission is possible only at specified voltages. The non-monotonic behavior of conductivity in the region below 33 V and above 41 V is probably due to changes in the transmission through the QPCs (inset, Figure 12c).

All the above studies are based on converting conducting graphene into a less conducting form through local anodic oxidation or etching.[78−84] Zhang et al., have reported a direct writing of graphene electronic devices using a catalytic AFM lithographic technique.[85] They have demonstrated the reduction of graphene oxide into graphene by the local electric field from the AFM tip in the presence of hydrogen.

The activation energy required for the reduction of GO can be significantly decreased by using a catalyst and a reactive gas such as H_2. Pt-coated AFM tip was chosen as a catalytic probe for the local reduction of GO into GNR in the presence of H_2 gas at a temperature of 115 °C under atmospheric pressure. The monolayer GO sheet was coated on an insulating substrate and connected to a gold pad for the electrical connectivity (see Figure 13a). After scanning the AFM tip on the sample at 100 °C in the presence of hydrogen gas (loading force of 10 nN and a scanning speed of 1 nm/s), a strip of graphene with a width of 80 nm and 2 μm long (see topographical images in Figure 13b, c) was formed. They have achieved GNRs with widths ranging from 20 to 80 nm with conductivities >1 × 10^4 S/m. The cAFM map showed a very bright contrast of the GNR, measured under a bias voltage of 2 V between the gold electrodes and the conducting tip scanned over the area in Figure 13d. This indicates that the GNR is conductive when compared with the rest of the insulating GO region. The electrical nature of the fabricated GNR was measured by recording current−voltage (I−V) characteristics at different positions on the GNR (see Figure 13e). The resistance (R) of the GNR was found to be varying linearly with distance between it and Au electrode (see inset of Figure 13e). Thus, the reduction of GO at the nanoscale seems to be an attractive approach for obtaining conducting graphene strips in a controlled manner. As this method involves mild operating conditions such as atmospheric pressure and relatively low temperatures, this may be a viable method for fabricating graphene based electronic devices for flexible applications.[85]

4. ELECTROSTATIC CHARGING OF CARBON NANOSTRUCTURES

A biased AFM tip has also been employed to induce and write charge patterns on a variety of carbon nanomaterials such as carbon nanotubes, graphene and fluorocarbon films. This technique is also called charge writing, which could be useful for fabricating local p−n junctions through electrostatic doping. Charge patterns on a surface could also become sites for clamping active molecules through electrostatic interactions.

4.1. Charging of Carbon Nanotubes. Zdrojek et al., have employed a biased AFM tip as a local tool for charging carbon nanotubes (single, double and multiwalled CNTs) supported on a SiO_2 substrate.[86]

The AFM topography of a typical CNT with a diameter of 19 nm is shown in Figure 14a. Before charge injection, Electrostatic Force Microscopy (EFM) was recorded with V_{EFM} of −3 V at a lift scan height of 100 nm (see Figure 14b). The dark contrast corresponds to the attractive capacitive interaction between the biased AFM tip and uncharged CNT. Charge was injected by contacting the AFM tip (V_{inj} = −5 V) for 2 min at the point on the CNT indicated by the arrow in Figure 14a. The resulting EFM image of the CNT after charging is shown in Figure 14c. The bright contrast is a repulsive interaction between the CNT and the negatively biased AFM tip (V_{EFM} = −3 V). This indicates that a negatively biased AFM tip could locally inject charge that spreads over many micrometers, spanning across the entire length of CNT (Figure 14c). The full width half maximum and magnitude of frequency shift is more for the charged CNT compared to the uncharged CNT (Figure 14d). Prisbrey et al., have demonstrated that writing charge patterns using an AFM tip in close proximity to carbon nanotube could move the Fermi level by 1 eV.[87] The substrate charge can be erased and rewritten, allowing electrostatic doping profiles which reconfigure a field-effect transistor into a p−n junction. Thus, the AFM charge lithography has the ability to controllably and reversibly modulate the doping profiles in nanoscale electronic and optoelectronic devices which will enable a variety of new investigations.[86,87]

4.2. Charge Injection in Graphene. Verdaguer et al., have shown that charge injection on isolated graphene sheets deposited on SiO_2/Si wafers, can be characterized using Kelvin probe force microscopy (KPFM).[88] The discharge process was induced by water under controlled ambient conditions.

Graphene was mechanically exfoliated and deposited on SiO_2/Si substrate before a biased AFM tip was used to inject charges on the isolated graphene sheets. Charge injection was performed on FLG film present over the grounded silicon substrate. The

dx.doi.org/10.1021/am500122g | ACS Appl. Mater. Interfaces 2014, 6, 6147−6163

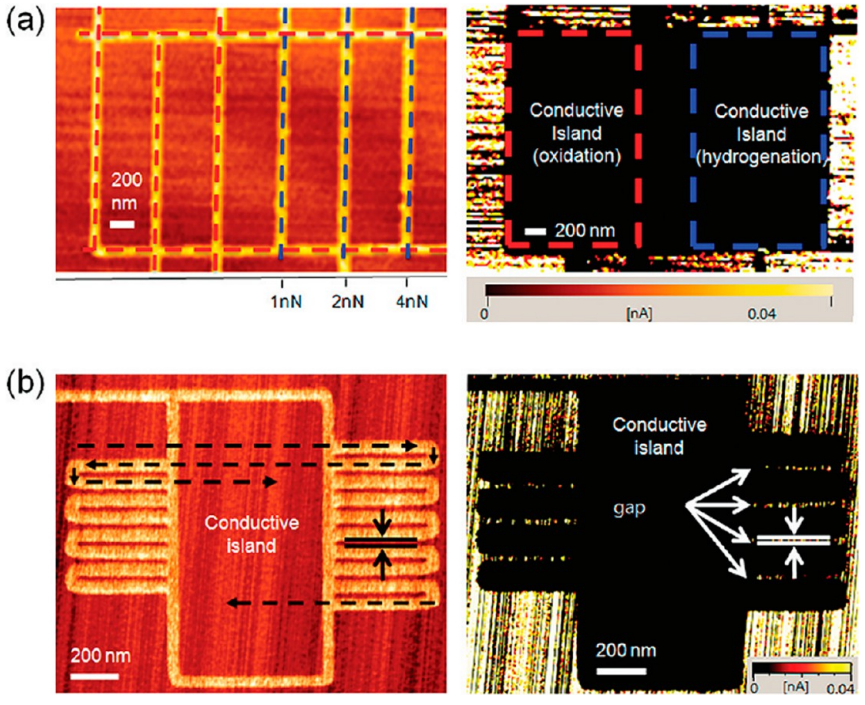

Figure 11. Oxidation and reduction of monolayer graphene using positive and negative sample biases to create electrically isolated regions. (a) Friction force microscopy (FFM) (left) and cAFM (right) images of graphene with hydrogenated (blue) or oxidized lines (red). (b, left) FFM and (b, right) cAFM images of the regions formed by insulating oxidized lines with sub-20 nm conducting gaps. Reprinted with permission from ref 83. Copyright 2011 American Chemical Society.

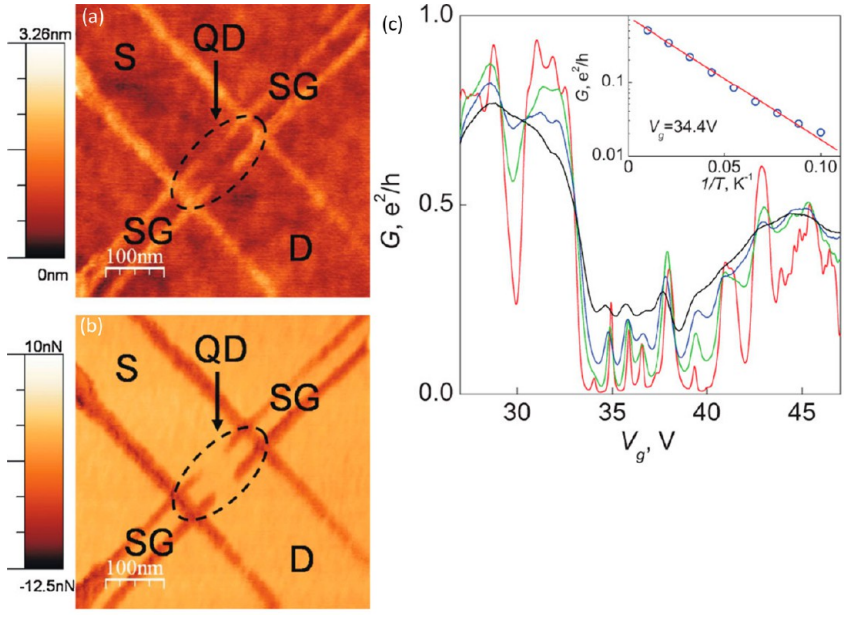

Figure 12. Graphene quantum dot (QD) structure fabricated by local anodic oxidation AFM. (a) Topography of a QD. (b) Corresponding friction image. Bright regions correspond to the pristine graphene and dark regions are the oxidized regions. The QD, source (S), drain (D), and side gates (SG) are formed with graphene and indicated in a and b. (c) Quantum conductance through QD structure (size ~100 nm) as a function of backgate voltage (V_g) for different temperatures (2.5, 10, 20, and 30 K are shown with red, green, blue, and black curves, respectively). Inset, temperature dependence of the conductivity at a minimum between peaks (V_g = 34.4 V). Reprinted with permission from ref 84. Copyright 2010 Wiley−VCH.

topography of the FLG film was obtained in contact mode before the charging process (top left, Figure 15a). Then, the tip was brought into contact at the center of the FLG film with a bias of V_{inj}, within the −10 to 10 V range (top right, Figure 15a). After a few minutes, the tip was retracted to about 200 nm from the surface, keeping the tip biased (lower left, Figure 15a). Once the tip is retracted from the surface, V_{inj} on the tip is switched off and a dual SPFM+KPM image is taken (lower right, Figure 15a). Using this method, one can guarantee noncontact conditions on the FLG film throughout the experiment and avoid the formation of a water neck between the tip and the sample that would perturb the discharge process. Charges were injected by

dx.doi.org/10.1021/am500122g | ACS Appl. Mater. Interfaces 2014, 6, 6147−6163

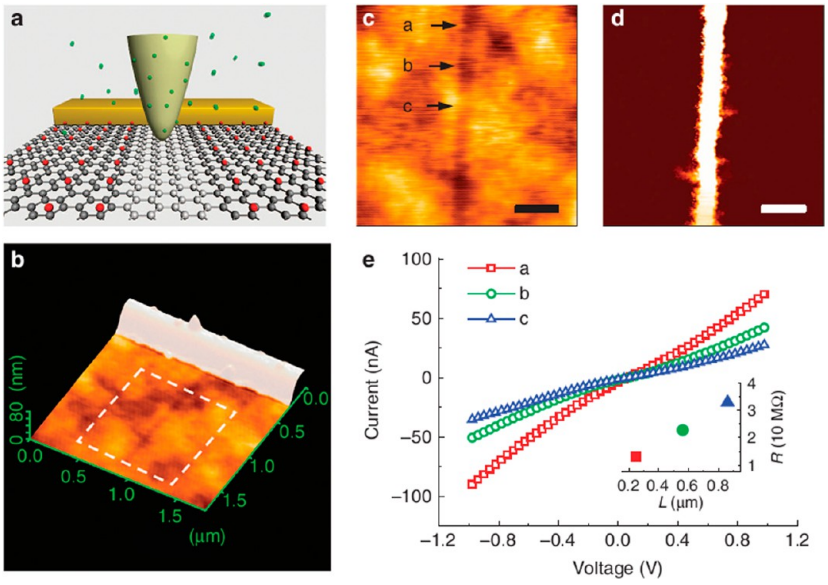

Figure 13. Local reduction graphene oxide (GO) to obtain GNRs via the catalytic scanning probe lithography (cSPL) (a) Schematic showing the setup of the cSPL in H_2 environment with a substrate temperature of 100 °C. (b) 3D topographical AFM image of the GNR obtained after writing on GO sheet (c) Topographical image and (d) current map of the marked area in b recorded at a sample bias of 2 V. (e) The $I-V$ curves of the GNR at different spots (three spots marked in c); the inset shows the resistance of the GNR with length. Scale bar, 200 nm. Reprinted with permission from ref 85. Copyright 2012 Nature Publishing Group.

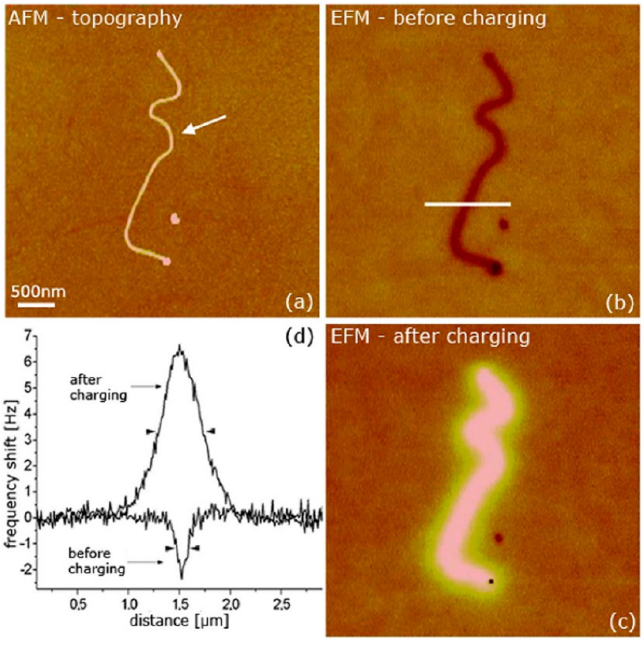

Figure 14. (a) Topography of MWNT (diameter, ~19 nm) on a 200 nm silicon dioxide surface. EFM images (b) before and (c) after charge injection at −5 V for 2 min. $V_{EFM} = -3$ V, lift scan height of 100 nm were used. (d) Frequency shift profiles for the MWNT before and after charge injection. Reprinted with permission from ref 86. Copyright 2006 American Institute of Physics.

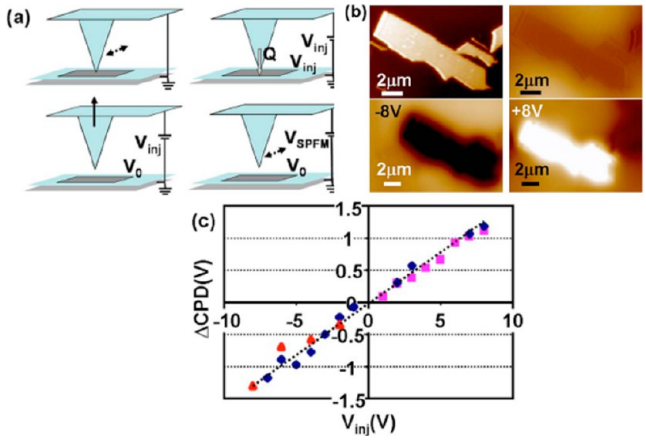

Figure 15. (a) Schematic showing charge injection and measurement on graphene using AFM. (b) AFM topography (top left) and KPFM (top right) images of a few layer graphene (FLG) film before charging at low RH. Bottom: KPFM images of the same film after charging to −8 V and +8 V. (c) Difference in the contact potential difference (ΔCPD) vs voltage applied to the tip during the charging process (V_{inj}) measured from KPFM taken after charge injection. Different symbols correspond to the measurements with different tips and samples. All experiments were performed at RH of 5%. Reprinted with permission from ref 88. Copyright 2009 American Institute of Physics.

contacting the AFM tip to the graphene sheets at V_{inj} of −8 and +8 V, respectively (Figure 15b), compare with before charging.

The difference in the contact potential difference (ΔCPD) is directly proportional to V_{inj} (see Figure 15c). ΔCPD measurements can get influenced by different contributions during the charging process such as contact and geometry of the tip-FLG system and also discharging of the FLG film with RH, during the retraction of the tip. The behavior of ΔCPD vs V_{inj} is linear indicating that the electrical contact between the tip and the FLG film is good enough with negligible loss of charge during injection. Electrical discharge was controlled through humidity conditions. Shen et al. employed the biased AFM tip to charge reduced graphene oxide (rGO) sheets and observed that the charge storage on rGO sheets is highly dependent on the reduction degree of the GO sheets.[89] By employing positive or negative tip biases, the rGO sheets were charged accordingly. Such charged nanostructures with pre-designated geometry could be helpful in constructing charge gated graphene nanoelectronics.

4.3. Charged Mesoscopic Graphitic Islands. In another study, it was found that the local electrochemical etching of a graphite surface to etch isolated shapes could, in addition, also store charge.

AFM bias lithography was used to etch hexagonal islands of varied lateral dimensions (see topography in Figure 16a). The

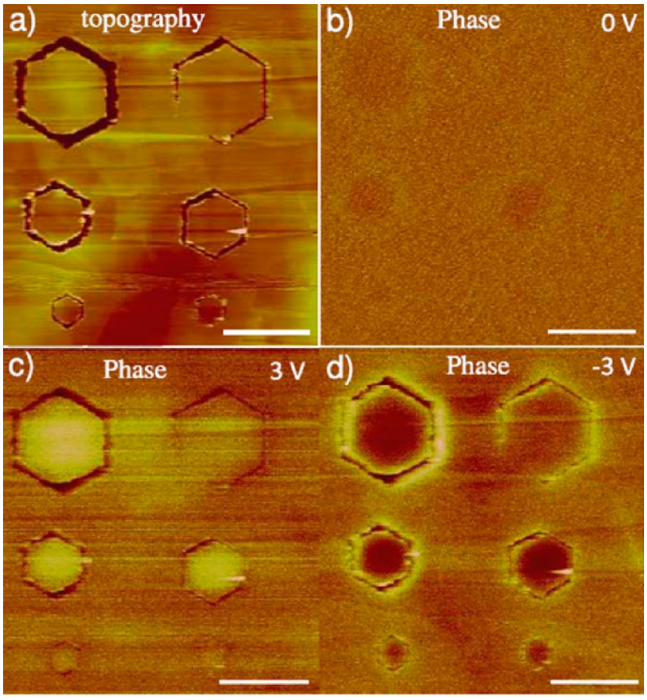

Figure 16. (a) Topography of hexagonal graphitic islands with lateral dimensions of 500 nm (top pair of hexagons), 300 nm (middle pair), and 150 nm (bottom pair), depths of 2−5 nm, fabricated using AFM. EFM phase images obtained with a tip bias of (b) 0, (c) 3, and (d) −3 V. Scale bar, 0.5 μm. Reprinted with permission from ref 34. Copyright 2011 Institute of Physics.

EFM phase images showed attractive/repulsive (negative/positive phase shifts) interactions with respect to the polarity of V_{EFM} , indicating that the isolated regions store positive charges (see Figure 16bc, d). This study showed that electrochemically etched hexagonal islands on graphite surface could hold charges deposited during the lithography process.

4.4. Charge Writing on Fluorocarbon Films. A biased AFM tip can also be used to directly write charge patterns on a surface through a process which is called charge lithography.[56] Thus, charge patterns written on surfaces can act as templates for attaching specific molecules through electrostatic interactions, giving rise to a new technique, called nanoxerography. To date, polymers and electret films have been employed for writing charge patterns employing this technique.

Fluorocarbon films seem like ideal substrates for writing charge patterns, which can't be detected in topographic images. The initial morphology of the fluorocarbon film on Si is smooth and featureless (see Figure 17a). The charge patterns were created by applying voltage pulses of 20 V for 50 μs. KPFM images show the charge patterns on the surface (see Figure 17b). The lateral resolution of the charge structure is 200 nm and the measured potential amounts to 200 mV.

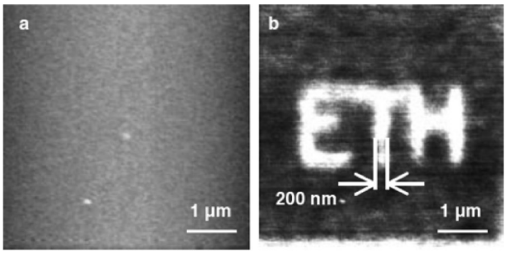

Figure 17. (a) Topography and (b) surface potential images of the charge patterns on the fluorocarbon layer (thickness of 10 nm). Reprinted with permission from ref 56. Copyright 2002 John Wiley & Sons.

5. MECHANICAL SCRATCHING OF GRAPHENE

AFM tip has also been used as local mechanical probe to cut the graphene sheets without application of voltage bias. Reduced graphene oxide sheets have been cut by AFM scratching technique.[90] Recently, graphene has been scratched to form nanogap electrodes, utilized in fabricating organic FETs and photoswitchers. Thus, AFM nanolithography technique could be a promising approach in making nanogap electrodes, crucial for molecular electronics.[91]

Graphene sheet was cut using AFM scratching technique to form nanogap electrodes (see Figures 18a and b). Active

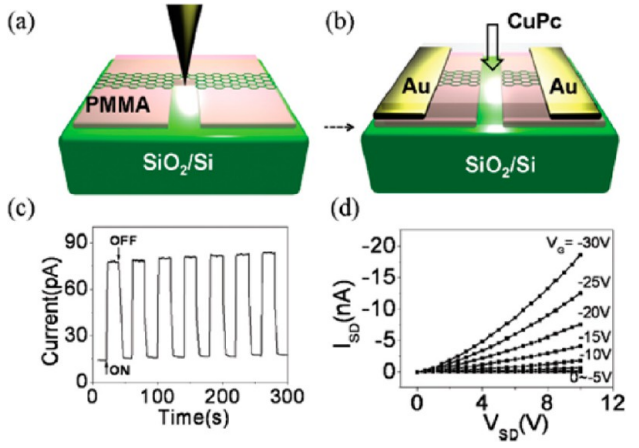

Figure 18. (a) Schematic diagram of graphene nanogap electrodes; (b) schematic structure of CuPc devices based on graphene nanogap electrodes; (c) photoswitching characteristics of the nanogap devices white light, light density 5.76 mw/cm^2, V = 1.0 V; (d) output characteristics of the CuPc organic field effect transistors. Reprinted with permission from ref 91. Copyright 2010 American Institute of Physics.

molecular species such as copper phthalocyanine (CuPc) were then vacuum deposited across the graphene nanogap electrodes. The photoconducting and field effect characteristics of the CuPc were investigated using graphene nanogap electrodes (see Figure 18c, d). Thus, AFM scratching technique could be a potential technique for fabricating molecular electronic devices.

6. CONCLUSIONS

This review presents an overview of scanning probe bias lithography with a focus on various carbon materials which undergo local electrochemical modifications and electrostatic charge storage events. It is clear that scanning probe nanolithographies based on the confinement of chemical reactions

offer a low-cost approach for academic research to fabricate nanometer-scale devices and to investigate fundamental electronic and chemical processes at the nanoscale. Because probe-based anodic oxidation can fabricate nanoscale devices directly without any resist based techniques, it has a distinct advantage of elimination of high end infrastructure. Scanning probe bias lithography has become an eye catching technique due to distinct advantages when compared to other lithographic techniques such as photolithography, e-beam lithography and plasma etching techniques. The unique capability of scanning probes has indeed led to the fabrication of several nanoscale devices which may not have been realized using other means. The fabrication of graphene-based nanodevices such as nanoribbons, nanorings and graphene quantum dots using probe-based oxidation techniques exhibit fundamental quantum phenomena such as quantum conductance or conductance fluctuations.

Between STM and AFM techniques, the latter has found wide spread use because of ease of operation, choice of substrates, speed, and reliable patterning. AFM-based charging of carbon nanostructures promotes the selective attachment of functional molecules through electrostatic interactions. This capability may lead to the development of nanocarbon surfaces in applications such as nanoxerography. Further, employing water as an electrolyte, the formation of various solvent molecular bridges between the tip and substrate may allow further control on the local modification of surfaces in a desired fashion. For example, graphene based transistors may not be suitable for logic applications due to poor on/off ratio of the devices. With SPM lithography, one can carve GNRs or functionalized graphene based transistors which exhibit better on/off ratios suitable for the real applications.[15] SPM bias lithography is also a viable approach for creating nanoscale Janus surfaces (local hydrophilic/hydrophobic regions) of graphene-like moieties. Bias lithography on carbon surfaces is not only limited to the water meniscus but also various other types of menisci have been tried out to create desired local functionality. Etching of the graphene nanoribbons may leave uneven edge structures which may cause degradation in the mobility of the GNRs; the edges can be made smooth by reducing the functional groups decorated at the edges using positively biased AFM tip. Because carbon is hydrophobic, one can make hydrophilic patterns in a selective manner to adsorb specific molecules and study charge transfer interactions. By writing charge patterns on graphene based materials, it may be possible to create anchoring sites for specific molecules via electrostatic clamping, providing yet another way to influence the local electronic structure of nanocarbons. This method may also offer a way to fabricate local p−n junctions in order to exercise a control on the electronic properties of carbon based systems. Another possibility is the fabrication of nanocarbon heterostructures combining with other functional materials (inorganic, organic, or bio), which may have promising electronic and optoelectronic properties. These heterostructures can be fabricated employing a combination of SPM with DPN or nanoimprint lithography techniques. SPM lithography has the potential capability to structure van der Waals solids (2D layered materials) with metal or semiconducting nanoparticles for nanoplasmonic applications. The driving force is the realization of photon coupling to charge at metal interfaces allows sub-diffraction localization of light which has revived the field of surface plasmons. Thus, SPM lithography can also be explored with the other techniques in fabricating graphene nanoplasmonic devices.[92]

Besides the role of local modifying tool, SPM can be employed as a measuring tool for studying the interaction and influence of specific molecules on carbon surfaces. The adsorption of water nanodroplets on hydrophobic surfaces is of current interest as it enables control of the local electronic properties of nanocarbons. It was reported that the nanodroplets could get adsorbed at the surface defects and step-edges, leading to wetting all the hydrophobic substrates similar to that of hydrophilic surfaces.[93,94] It was also reported that the adsorption of water at the defect sites of the nanocarbons, make them p-type material as the water molecules suppress the electron conduction.[95] The adsorbed water could also change the workfunction of the nanocarbons as much as 1 eV,[96] one of the simplest ways to tune the electronic properties.

Because AFM is mostly serial in nature, only prototype devices have been made so far. The biggest challenge, therefore, is its low throughput. Nonetheless, the rapid development of video rate AFMs promise fast fabrication of nano-scale or quantum devices over a large area in a single processing step. The advancement is due to (i) novel, ultrasmall cantilever fabrication, and (ii) improved scanning system design. Reports indicate scanning 10 000 times faster than commercial AFMs are possible.[97] Even, AFM technique can also be made as an effective parallel technique by employing millipede tips to fabricate an array of nanoscale devices after addressing the issues of reliability and overall integration of the system.[98] Other possibility is to use AFM in combination with techniques such as photolithography, electron beam lithography or nanoimprint lithography (NIL), and enable nanoscale devices fabrication under ambient conditions. For, example, SPM/NIL approach is a viable approach for fabricating planar FETs in which channel is surrounded by gate unlike non planar FETs.[99,100] One can improve throughput drastically by employing parallel array of probes which are self-actuated with self-sensing capability. This may be possible through designing nanoimprint molds with feature sizes of the order of sub-5 nm employing AFM based closed loop lithography. This can eventually lead us to envisage a transition from classical FET devices to quantum-effect devices at the nanometer scale. The exploration of practical application of quantum-dot and single-electron devices may open up the gate way for "beyond CMOS" nanoelectronic devices.[100] Further progress in AFM nanolithography therefore relies almost entirely on methods to improve speed and reliability for mass production. Future efforts in SPM may bring in a better understanding of the surface phenomena particularly in relation to "writing" on nanocarbon materials.

AUTHOR INFORMATION

Corresponding Authors

*E-mail: kulkarni@jncasr.ac.in.
*E-mail: reifenbr@purdue.edu.

Author Contributions

The manuscript was written through contributions of all authors. All authors have given approval to the final version of the manuscript.

Notes

The authors declare no competing financial interest.

ACKNOWLEDGMENTS

The authors thank Professor C. N. R. Rao, FRS, for his encouragement. Support from the Department of Science and Technology, Government of India, is gratefully acknowledged.

N.K. acknowledges CSIR for funding. G.U.K. acknowledges the Sheikh Saqr Senior Fellowship.

DEDICATION

Dedicated to Prof. Giridhar U. Kulkarni on the occasion of his 50th birthday.

REFERENCES

(1) Robertson, J. Hard Amorphous (Diamond-like) Carbons. *Prog. Solid State Chem.* **1991**, *21*, 199−333.
(2) Robertson, J. Diamond-like Carbon. *Pure Appl. Chem.* **1994**, *66*, 1789−1796.
(3) Dresselhaus, M. S.; Dresselhaus, G.; Eklund, P. C. *Science of Fullerenes and Carbon Nanotubes*: Academic Press: NewYork, 1996.
(4) Geim, A. K.; Novoselov, K. S. The Rise of Graphene. *Nat. Mater.* **2007**, *6*, 183−191.
(5) Wei, D.; Liu, Y. Controllable Synthesis of Graphene and Its Applications. *Adv. Mater.* **2010**, *22*, 3225−3241.
(6) Bonnell, D. *Scanning Probe Microscopy and Spectroscopy*; Ed.; Wiley-VCH: New York, 2000.
(7) Binnig, G.; Quate, C. F.; Gerber, C. Atomic Force Microscope. *Phys. Rev. Lett.* **1986**, *56*, 930−933.
(8) Nyffenegger, R. M.; Penner, R. M. Nanometer-Scale Surface Modification Using the Scanning Probe Microscope: Progress Since 1991. *Chem. Rev.* **1997**, *97*, 1195−1230.
(9) Wouters, D.; Schubert, U. S. Nanolithography and Nanochemistry: Probe-Related Patterning Techniques and Chemical Modification for Nanometer-Sized Devices. *Angew. Chem., Int. Ed.* **2004**, *43*, 2480−2495.
(10) Xie, X. N.; Chung, H. J.; Sow, C. H.; Wee, A. T. S. Nanoscale Materials Patterning and Engineering by Atomic Force Microscopy Nanolithography. *Mater. Sci. Eng., R* **2006**, *54*, 1−48.
(11) Garcia, R.; Martinez, R. V.; Martinez, J. Nano-chemistry and Scanning Probe Nanolithographies. *Chem. Soc. Rev.* **2006**, *35*, 29−38.
(12) Salaita, K.; Wang, Y.; Mirkin, C. A. Applications of Dip-Pen Nanolithography. *Nat. Nanotechnol.* **2007**, *2*, 145−155.
(13) Ginger, D. S.; Zhang, H.; Mirkin, C. A. The Evolution of Dip-Pen Nanolithography. *Angew. Chem., Int. Ed.* **2004**, *43*, 30−45.
(14) Piner, R. D.; Zhu, J.; Xu, F.; Hong, S.; Mirkin, C. A. "Dip-Pen" Nanolithography. *Science* **1999**, *283*, 661−663.
(15) Geim, A. K. Nobel Lecture: Random Walk to Graphene. *Rev. Mod. Phys.* **2011**, *83*, 851−862.
(16) Pimenta, M. A.; Dresselhaus, G.; Dresselhaus, M. S.; Cancado, L. G.; Jorio, A.; Saito, R. Studying Disorder in Graphite-based Systems by Raman Spectroscopy. *Phys. Chem. Chem. Phys.* **2007**, *9*, 1276−1290.
(17) Ferrari, A. C.; Robertson, J. Interpretation of Raman Spectra of Disordered and Amorphous Carbon. *Phys. Rev. B* **2000**, *61*, 14095−14107.
(18) Biró, L. P.; Nemes-Incze, P.; Lambin, P. Graphene: Nanoscale Processing and Recent Applications. *Nanoscale* **2012**, *4*, 1824−1839.
(19) Verdaguer, A.; Sacha, G. M.; Bluhm, H.; Salmeron, M. Molecular Structure of Water at Interfaces: Wetting at the Nanometer Scale. *Chem. Rev.* **2006**, *106*, 1478−1510.
(20) Xu, L.; Salmeron, M. In *Nano-surface Chemistry*; M. Rosoff, Ed.; Dekker: New York, 2001; pp 243−287.
(21) Stifter, T.; Marti, O.; Bhushan, B. Theoretical Investigation of the Distance Dependence of Capillary and van der Waals Forces in Scanning Force Microscopy. *Phys. Rev. B* **2000**, *62*, 13667−13673.
(22) Cappella, B.; Dietler, G. Force-Distance Curves by Atomic Force Microscopy. *Surf. Sci. Rep.* **1999**, *34*, 1−104.
(23) Jang, J.; Schatz, G. C.; Ratner, M. A. How Narrow Can a Meniscus Be? *Phys. Rev. Lett.* **2004**, *92*, 085504.
(24) Kohonen, M. M.; Maeda, N.; Christenson, H. K. Kinetics of Capillary Condensation in a Nanoscale Pore. *Phys. Rev. Lett.* **1999**, *82*, 4667−4670.
(25) Paramonov, P. V.; Lyuksyutov, S. F. Density-Functional Description of Water Condensation in Proximity of Nanoscale Asperity. *J. Chem. Phys.* **2005**, *123*, 084705.
(26) van Honschoten, J. W.; Brunets, N.; Tas, N. R. Capillarity at the Nanoscale. *Chem. Soc. Rev.* **2010**, *39*, 1096−1114.
(27) Nosonovsky, M.; Bhushan, B. Phase Behavior of Capillary Bridges: Towards Nanoscale Water Phase Diagram. *Phys. Chem. Chem. Phys.* **2008**, *10*, 2137−2144.
(28) Israelachvili, J. N. *Intermolecular and Surface Forces: With Applications to Colloidal and Biological Systems*, 3rd ed.; Academic: New York, 1998.
(29) Weeks, B. L.; Vaughn, M. W.; DeYoreo, J. J. Direct Imaging of Meniscus Formation in Atomic Force Microscopy Using Environmental Scanning Electron Microscopy. *Langmuir* **2005**, *21*, 8096−8098.
(30) Schenk, M.; Füting, M.; Reichelt, R. Direct Visualization of the Dynamic Behavior of a Water Meniscus by Scanning Electron Microscopy. *J. Appl. Phys.* **1998**, *84*, 4880.
(31) Orr, F. M.; Scriven, L. E.; Rivas, A. P. Pendular Rings between Solids: Meniscus Properties and Capillary Forces. *J. Fluid Mech.* **1975**, *67*, 723−742.
(32) Fisher, L. R.; Israelachvili, J. N. Experimental Studies on the Applicability of the Kelvin Equation to Highly Curved Concave Menisci. *J. Colloid Interface Sci.* **1981**, *80*, 528−541.
(33) Braslavskya, I.; Lipson, S. G. Electrofreezing Effect and Nucleation of Ice Crystals in Free Growth Experiments. *Appl. Phys. Lett.* **1998**, *72*, 264−266.
(34) Kurra, N.; Gyan, P.; Basavaraja, S.; Timothy, S. F.; Kulkarni, G. U.; Ronald, G. R. Charge Storage in Mesoscopic Graphitic Islands Fabricated using AFM Bias Lithography. *Nanotechnology* **2011**, *22*, 245302.
(35) Calleja, M.; Tello, M.; García, R. Size Determination of Field-Induced Water Menisci in Noncontact Atomic Force Microscopy. *J. Appl. Phys.* **2002**, *92*, 5539−5542.
(36) Sacha, G. M.; Verdaguer, A.; Salmeron, M. Induced Water Condensation and Bridge Formation by Electric Fields in Atomic Force Microscopy. *J. Phys. Chem. B* **2006**, *110*, 14870−14873.
(37) Cramer, T.; Zerbetto, F.; García, R. Molecular Mechanism of Water Bridge Buildup: Field-Induced Formation of Nanoscale Menisci. *Langmuir* **2008**, *24*, 6116−6120.
(38) Gómez-Moñivas, S.; Sáenz, J. J.; Calleja, M.; García, R. Field-Induced Formation of Nanometer-Sized Water Bridges. *Phys. Rev. Lett.* **2003**, *91*, 56101.
(39) Kurra, N.; Scott, A.; Kulkarni, G. U. Electrocondensation and Evaporation of Attoliter Water Droplets: Direct Visualization Using Atomic Force Microscopy. *Nano Res.* **2010**, *3*, 307−316.
(40) Heinze, J. Ultramicroelectrodes in Electrochemistry. *Angew. Chem., Int. Ed.* **1993**, *32*, 1268−1288.
(41) Sugimura, H.; Nakagiri, N. Chemical Approach to Nano-fabrication: Modifications of Silicon Surfaces Patterned by Scanning Probe Anodization. *Jpn. J. Appl. Phys.* **1995**, *34*, 3406−3411.
(42) Garcia, R.; Calleja, M.; Rohrer, H. Patterning of Silicon Surfaces with Noncontact Atomic Force Microscopy: Field-Induced Formation of Nanometer-Size Water Bridges. *J. Appl. Phys.* **1999**, *86*, 1898−1903.
(43) Dai, H.; Franklin, N.; Han, J. Exploiting the Properties of Carbon Nanotubes for Nanolithography. *Appl. Phys. Lett.* **1998**, *73*, 1508.
(44) Dagata, J.; Schneir, J.; Harary, H. H.; Evans, C. J.; Postek, M. T.; Bennett, J. Modification of Hydrogen-Passivated Silicon by a Scanning Tunneling Microscope Operating in Air. *Appl. Phys. Lett.* **1990**, *56*, 2001.
(45) Day, H. C.; Allee, D. R. Selective Area Oxidation of Silicon with a Scanning Force Microscope. *Appl. Phys. Lett.* **1993**, *62*, 2691−2693.
(46) Minne, S. C.; Soh, H. T.; Flueckiger, Ph.; Quate, C. F. Fabrication of 0.1 μm Metal oxide Semiconductor Field-Effect Transistors with the Atomic Force Microscope. *Appl. Phys. Lett.* **1995**, *66*, 703−705.
(47) Martel, R.; Schmidt, T.; Sandstrom, R. L.; Avouris, Ph. Current-Induced Nanochemistry: Local Oxidation of Thin Metal Films. *J. Vac. Sci. Technol. A* **1999**, *17*, 1451−1456.
(48) Lyuksyutov, S. F.; Vaia, R. A.; Paramonov, P. B.; Juhl, S.; Waterhouse, L.; Ralich, R. M.; Sigalov, G.; Sancaktar, E. Electrostatic Nanolithography in Polymers using Atomic Force Microscopy. *Nat. Mater.* **2003**, *2*, 468−472.

(49) Vijaykumar, T.; Kulkarni, G. U. Electrostatic Nanolithography on PVP Films for Patterning Metal Nanocrystals and Fullerenes. *Nanotechnology* **2007**, *18*, 445303.
(50) Reagan, M. A.; Kashyn, D.; Juhl, S.; Vaia, R. A.; Lyuksyutov, S. F. Electric Charging and Nanostructure Formation in Polymeric Films using Combined Amplitude-Modulated Atomic Force Microscopy-Assisted Electrostatic Nanolithography and Electric Force Microscopy. *Appl. Phys. Lett.* **2008**, *93*, 033109.
(51) Xie, X. N.; Chung, H. J.; Liu, Z. J.; Yang, S.-W.; Sow, C. H.; Wee, A. T. S. A New Scenario in Probe Local Oxidation: Transient Pressure-Wave-Assisted Ionic Spreading and Oxide Pattern Formation. *Adv. Mater.* **2007**, *19*, 2618−2623.
(52) Xie, X. N.; Chung, H. J.; Sow, C. H.; Adamiak, K.; Wee, A. T. S. Electrical Discharge in a Nanometer-Sized Air/Water Gap Observed by Atomic Force Microscopy. *J. Am. Chem. Soc.* **2005**, *127*, 15562−15567.
(53) Xie, X. N.; Deng, M.; Xu, H.; Yang, S. W.; Qi, D. C.; Gao, X. Y.; et al. Creating Polymer Structures of Tunable Electric Functionality by Nanoscale Discharge-Assisted Cross-Linking and Oxygenation. *J. Am. Chem. Soc.* **2006**, *128*, 2738−2744.
(54) Mesquida, P.; Stemmer, A. Attaching Silica Nanoparticles from Suspension onto Surface Charge Patterns Generated by a Conductive Atomic Force Microscope Tip. *Adv. Mater.* **2001**, *13*, 1395−1398.
(55) Ressier, L.; Nader, V. L. Electrostatic Nanopatterning of PMMA by AFM Charge Writing for Directed Nano-Assembly. *Nanotechnology* **2008**, *19*, 135301.
(56) Mesquida, P.; Knapp, H. F.; Stemmer, A. Charge Writing on the Nanometre Scale in a Fluorocarbon Film. *Surf. Interface Anal.* **2002**, *33*, 159−162.
(57) Xie, Y.; Bell, C.; Yajima, T.; Hikita, Y.; Hwang, H. Y. Charge Writing at the $LaAlO_3/SrTiO_3$ Surface. *Nano Lett.* **2010**, *10*, 2588−2591.
(58) Albrecht, T. R.; Dovek, M. M.; Kirk, M. D.; Lang, C. A.; Quate, C. F.; Smith, D. P. E. Nanometer-Scale Hole Formation on Graphite using a Scanning Tunneling Microscope. *Appl. Phys. Lett.* **1989**, *55*, 1727−1729.
(59) Mizutani, W.; Inukai, J.; Ono, M. Making a Monolayer Hole in a Graphite Surface by means of a Scanning Tunneling Microscope. *Jpn. J. Appl. Phys.* **1990**, *29*, L815−L817.
(60) McCarley, R. L.; Hendricks, S. A.; Bard, A. J. Controlled Nanofabrication of Highly Oriented Pyrolytic Graphite with the Scanning Tunneling Microscope. *J. Phys. Chem.* **1992**, *96*, 10089−10092.
(61) Park, J. G.; Zhang, C.; Liang, R.; Wang, B. Nano-machining of Highly Oriented Pyrolytic Graphite using Conductive Atomic Force Microscope Tips and Carbon Nanotubes. *Nanotechnology* **2007**, *18*, 405306.
(62) Jiang, Y.; Guo, W. Convex and Concave Nanodots and Lines Induced on HOPG Surfaces by AFM Voltages in Ambient Air. *Nanotechnology* **2008**, *19*, 345302.
(63) Yoshimizu, N.; Hicks, B.; Lal, A.; Pollock, C. R. Scanning Probe Nanoscale Patterning of Highly Ordered Pyrolytic Graphite. *Nanotechnology* **2010**, *21*, 095306.
(64) Park, J.; Kim, K. B.; Park, J.-Y.; Choi, T.; Seo, Y. Graphite Patterning in a Controlled Gas Environment. *Nanotechnology* **2011**, *22*, 335304.
(65) Avramescu, A.; Ueta, A.; Uesugi, K.; Suemune, I. Atomic Force Microscope Lithography on Carbonaceous Films Deposited by Electron-Beam Irradiation. *Appl. Phys. Lett.* **1998**, *72*, 716−718.
(66) Mühl, T.; Brückl, H.; Weise, G.; Reiss, G. Nanometer-Scale Lithography in Thin Carbon Layers using Electric Field Assisted Scanning Force Microscopy. *J. Appl. Phys.* **1997**, *82*, 5255−5258.
(67) Kurra, N. Tunable Atomic Force Microscopy Bias Lithography on Electron Beam Induced Carbonaceous Platforms. *AIP Adv.* **2013**, *3*, 092108.
(68) Kurra, N.; Bhadram, V. S.; Narayana, C.; Kulkarni, G. U. Field-Effect Transistors Based on Thermally Treated Electron Beam-Induced Carbonaceous Patterns. *ACS Appl. Mater. Interfaces* **2012**, *4*, 1030−1036.
(69) Kim, D.-H.; Koo, J.-Y.; Kim, J.-J. Cutting of Multiwalled Carbon Nanotubes by a Negative Voltage Tip of an Atomic Force Microscope: A Possible Mechanism. *Phys. Rev. B* **2003**, *68*, 113406.
(70) Park, J.-Y.; Yaish, Y.; Brink, M.; Rosenblatt, S.; McEuen, P. L. Electrical Cutting and Nicking of Carbon Nanotubes using an Atomic Force Microscope. *Appl. Phys. Lett.* **2002**, *80*, 4446−4448.
(71) Collins, P. G.; Hersam, M.; Arnold, M.; Martel, R.; Avouris, P. Current Saturation and Electrical Breakdown in Multiwalled Carbon Nanotubes. *Phys. Rev. Lett.* **2001**, *86*, 3128−3131.
(72) Novoselov, K. S.; Geim, A. K.; Morozov, S. V.; Jiang, D.; Zhang, Y.; Dubonos, S. V.; et al. Electric Field Effect in Atomically Thin Carbon Films. *Science* **2004**, *306*, 666−669.
(73) Bunch, J. S.; van der Zande, A. M.; Verbridge, S. S.; Frank, I. W.; Tanenbaum, D. M.; Parpia, J. M.; et al. Electromechanical Resonators from Graphene Sheets. *Science* **2007**, *315*, 490−493.
(74) Ezawa, M. Peculiar Width Dependence of the Electronic Properties of Carbon Nanoribbons. *Phys. Rev. B* **2006**, *73*, 045432.
(75) Bai, J.; Duan, X.; Huang, Y. Rational Fabrication of Graphene Nanoribbons Using a Nanowire Etch Mask. *Nano Lett.* **2009**, *9*, 2083−2087.
(76) Liang, X.; Chang, A. S. P.; Zhang, Y.; Harteneck, B. D.; Choo, H.; Olynick, D. L.; et al. Electrostatic Force Assisted Exfoliation of Pre Patterned Few-Layer Graphenes into Device Sites. *Nano Lett.* **2008**, *9*, 467−472.
(77) Li, D.; Windl, W.; Padture, N. P. Toward Site-Specific Stamping of Graphene. *Adv. Mater.* **2009**, *21*, 1243−1246.
(78) Tapaszto, L.; Dobrik, G.; Lambin, P.; Biro, L. P. Tailoring the Atomic Structure of Graphene Nanoribbons by Scanning Tunneling Microscope Lithography. *Nat. Nanotechnol.* **2008**, *3*, 397−401.
(79) Alaboson, J. M. P.; Wang, Q. H.; Kellar, J. A.; Park, J.; Elam, J. W.; Pellin, M. J.; et al. Conductive Atomic Force Microscope Nanopatterning of Epitaxial Graphene on SiC(0001) in Ambient Conditions. *Adv. Mater.* **2011**, *23*, 2181−2184.
(80) Masubuchi, S.; Ono, M.; Yoshida, K.; Hirakawa, K.; Machida, T. Fabrication of Graphene Nanoribbon by Local Anodic Oxidation Lithography using Atomic Force Microscope. *Appl. Phys. Lett.* **2009**, *94*, 082107.
(81) Weng, L.; Zhang, L.; Chen, Y. P.; Rokhinson, L. P. Atomic Force Microscope Local Oxidation Lithography of Graphene. *Appl. Phys. Lett.* **2008**, *93*, 093107.
(82) Masubuchi, S.; Arai, M.; Machida, T. Atomic Force Microscopy Based Tunable Local Anodic Oxidation of Graphene. *Nano Lett.* **2011**, *11*, 4542−4546.
(83) Byun, I.-S.; Yoon, D.; Choi, J. S.; Hwang, I.; Lee, D. H.; Lee, M. J.; et al. Nanoscale Lithography on Monolayer Graphene Using Hydrogenation and Oxidation. *ACS Nano* **2011**, *5*, 6417−6424.
(84) Neubeck, S.; Ponomarenko, L. A.; Freitag, F.; Giesbers, A. J. M.; Zeitler, U.; Morozov, S. V.; et al. From One Electron to One Hole: Quasiparticle Counting in Graphene Quantum Dots Determined by Electrochemical and Plasma Etching. *Small* **2010**, *6*, 1469−1473.
(85) Zhang, K.; Fu, Q.; Pan, N.; Yu, X.; Liu, J.; Luo, Y.; Wang, X.; Yang, J.; Hou, J. Direct Writing of Electronic Devices on Graphene Oxide by Catalytic Scanning Probe Lithography. *Nat. Commun.* **2012**, *3*, 1194.
(86) Zdrojek, M.; Mélin, T.; Diesinger, H.; Stiévenard, D.; Gebicki, W.; Adamowicz, L. Charging and Discharging Processes of Carbon Nanotubes Probed by Electrostatic Force Microscopy. *J. Appl. Phys.* **2006**, *100*, 114326.
(87) Prisbrey, L.; DeBorde, T.; Park, J.-Y.; Minot, E. D. Controlling the Function of Carbon Nanotube Devices with Re-Writable Charge Patterns. *Appl. Phys. Lett.* **2011**, *99*, 053125.
(88) Verdaguer, A.; Cardellach, M.; Segura, J. J.; Sacha, G. M.; Moser, J.; Zdrojek, M.; Bachtold, A.; Fraxedas, J. Charging and Discharging of Graphene in Ambient Conditions Studied with Scanning Probe Microscopy. *Appl. Phys. Lett.* **2009**, *94*, 233105.
(89) Shen, Y.; Guo, S.; Hu, J.; Zhang, Y. Charging of Nanostructured and Partially Reduced Graphene Oxide Sheets. *Appl. Phys. Lett.* **2012**, *101*, 183109.

(90) Lu, G.; Zhou, X.; Li, H.; Yin, Z.; Li, B.; Huang, L.; et al. Nanolithography of Single-Layer Graphene Oxide Films by Atomic Force Microscopy. *Langmuir* **2010**, *26*, 6164−6166.
(91) He, Y.; Dong, H.; Li, T.; Wang, C.; Shao, W.; Zhang, Y.; Jiang, L.; Hu, W. Graphene and Graphene Oxide Nanogap Electrodes Fabricated by Atomic Force Microscopy Nanolithography. *Appl. Phys. Lett.* **2010**, *97*, 133301.
(92) Grigorenko, A. N.; Polini, M.; Novoselov, K. S. Graphene Plasmonics. *Nat. Photonics* **2012**, *6*, 749−758.
(93) Cao, P.; Xu, K.; Varghese, J. O.; Heath, J. R. The Microscopic Structure of Adsorbed Water on Hydrophobic Surfaces under Ambient Conditions. *Nano Lett.* **2011**, *11*, 5581−5586.
(94) Xu, K.; Cao, P.; Heath, J. R. Graphene Visualizes the First Water Adlayers on Mica at Ambient Conditions. *Science* **2010**, *329*, 1188−1191.
(95) Collins, P. G.; Bradley, K.; Ishigami, M.; Zettl, A. Extreme Oxygen Sensitivity of Electronic Properties of Carbon Nanotubes. *Science* **2000**, *287*, 1801−1804.
(96) Yavari, F.; Kritzinger, C.; Gaire, C.; Song, L.; Gulapalli, H.; Borca-Tasciuc, T.; Ajayan, P. M.; Koratkar, N. Tunable Bandgap in Graphene by the Controlled Adsorption of Water Molecules. *Small* **2010**, *6*, 2535−2538.
(97) Payton, O. D.; Picco, L.; Robert, D.; Raman, A.; Homer, M. E.; Champneys, A. R.; Miles, M. J. High-speed Atomic Force Microscopy in Slow Motion-understanding Cantilever Behavior at High Scan Velocities. *Nanotechnology* **2012**, *23*, 205704.
(98) Vettiger, P.; Cross, G.; Despont, M.; Drechsler, U.; Durig, U.; Gotsmann, B.; Häberle, W.; Lantz, M.A.; Rothuizen, H. E.; Stutz, R.; Binnig, G. K. The "Millipede"-Nanotechnology Entering Data Storage. *IEEE Trans. Nanotechnol.* **2002**, *1*, 39−55.
(99) Ong, H. G.; Wang, J. Study of Carbon Nanotube Based Devices Using Scanning Probe Microscope. In *Physical and Chemical Properties of Carbon Nanotubes*; Suzuki, S. , Ed.; Tech-Open Access Publisher: Rijeka, Croatia, 2013; pp 337−356.
(100) Durrani, Z.; Jones, M.; Kaestner, M.; Hofer, M.; Guliyev, E.; Ahmad, A.; Ivanov, T.; Zoellner, J.-P.; Rangelow, I. W. Scanning Probe Lithography Approach for Beyond CMOS Devices. *Proc. SPIE* **2013**, *8680*, 868017.